J. Fluid Mech. (2003), *vol.* 486, *pp.* 331–378.
DOI: 10.1017/S0022112003004749 Printed in the United Kingdom

Three-dimensional vortex breakdown in swirling jets and wakes: direct numerical simulation

By M. R. RUITH†[1], P. CHEN[1,2], E. MEIBURG[3] AND T. MAXWORTHY[1]

[1]Department of Aerospace and Mechanical Engineering, University of Southern California, Los Angeles, CA 90089, USA

[2]Yahoo! Inc. 3400 Central Expressway, Santa Clara, CA 95051, USA

[3]Department of Mechanical and Environmental Engineering, University of California, Santa Barbara, CA 93106, USA

(Received 12 July 2002 and in revised form 2 January 2003)

Vortex breakdown of nominally axisymmetric, swirling incompressible flows with jet- and wake-like axial velocity distributions issuing into a semi-infinite domain is studied by means of direct numerical simulations. By selecting a two-parametric velocity profile for which the steady axisymmetric breakdown is well-studied (Grabowski & Berger 1976), issues are addressed regarding the role of three-dimensionality and unsteadiness with respect to the existence, mode selection, and internal structure of vortex breakdown, in terms of the two governing parameters and the Reynolds number. Low Reynolds numbers are found to yield flow fields lacking breakdown bubbles or helical breakdown modes even for high swirl. In contrast, highly swirling flows at large Reynolds numbers exhibit bubble, helical or double-helical breakdown modes, where the axisymmetric mode is promoted by a jet-like axial velocity profile, while a wake-like profile renders the flow helically unstable and ultimately yields non-axisymmetric breakdown modes. It is shown that a transition from super- to subcritical flow, as defined by Benjamin (1962), accurately predicts the parameter combination yielding breakdown, if applied locally to flows with supercritical inflow profiles. Thus the basic form of breakdown is axisymmetric, and a transition to helical breakdown modes is shown to be caused by a sufficiently large pocket of absolute instability in the wake of the bubble, giving rise to a self-excited global mode. Two distinct eigenfunctions corresponding to azimuthal wavenumbers $m = -1$ and $m = -2$ have been found to yield a helical or double-helical breakdown mode, respectively. Here the minus sign represents the fact that the winding sense of the spiral is opposite to that of the flow.

1. Introduction

Vortex breakdown of swirling jets and wakes characterizes an abrupt change in the structure of the nominally axisymmetric core of a swirling flow, forming an internal stagnation point. Although vortex breakdown is also relevant for compressible,

† Author to whom correspondence should be addressed, present address: Department of Mechanical and Environmental Engineering, University of California, Santa Barbara, CA 93106, USA, ruith@engineering.ucsb.edu

turbulent, and even supersonic flows, the present investigation is limited to laminar and incompressible flows.

Vortex breakdown represents a crucial element in a variety of technical applications ranging from beneficial to detrimental. For example, in combustion swirl is frequently employed to achieve a large spreading angle of the jet, which leads to an upstream flow of the hot combustion products near the jet centreline and thereby serves to stabilize the flame (Beér & Chigier 1972). For the purpose of developing compact, efficient and non-polluting combustors, the governing fluid mechanical and chemical processes need to be optimized, which in turn requires a detailed understanding of the dynamical evolution of the swirling flow and its effect on and interaction with the combustion process and the flame structure. Further beneficial effects of vortex breakdown are enhanced mixing and the destruction of wake vortices behind aircrafts to increase the possible take-off frequency at airports. On the other hand, breakdown of the lift-generating vortices above a delta wing leads to an abrupt deterioration of the lift and drag characteristics and to poor controllability (Mitchell & Délery 2001). Furthermore, atmospheric conditions such as tornadoes, dust devils and water spouts give rise to swirling flows, potentially causing vortex breakdown.

In spite of extensive theoretical, numerical and experimental research over more than four decades (Benjamin 1962; Hall 1972; Leibovich 1978; Escudier, Bornstein & Maxworthy 1982; Escudier 1988; Althaus, Brücker & Weimer 1995*a*; Spall & Snyder 1999; Lucca-Negro & O'Doherty 2001; Delbende, Chomaz & Huerre 1998 and many others), no generally accepted explanation for the onset, internal structure, and mode selection of vortex breakdown has been found. Insufficient understanding of the phenomenon causes poor effectiveness of the techniques applied to control vortex breakdown, cf. Mitchell & Délery (2001). These authors observe that decisive progress toward achieving swirling flows that are reliably tailored to desired operating conditions requires further basic investigations in order to unravel the underlying fluid dynamics.

The accurate numerical simulation of nominally axisymmetric, swirling flows exhibiting vortex breakdown is particularly demanding, since it requires the solution of the full Navier–Stokes equations in cylindrical coordinates for three-dimensional, unsteady flow. Casting the Navier–Stokes equations in cylindrical coordinates requires special care due to the singular behaviour of some terms near the axis. From the point of view of specifying conditions at the open boundaries, this class of flows is particularly challenging due to its ability to support travelling waves, which renders the flow particularly sensitive to small disturbances. Further, it has been found that prescribing an axial pressure gradient far away radially from the vortex can determine the onset of vortex breakdown and govern its mode selection, cf. review articles by Althaus *et al.* (1995*a*) and Spall & Snyder (1999).

Furthermore, the fact that swirling flows allow two competing and interacting instability mechanisms in the form of a shear layer and centrifugal instability adds to the complexity of the problem. Thus the vortex breakdown phenomenon has proven to be a formidable challenge for fundamental theories.

The concept of hydrodynamic instability as the reason for vortex breakdown, developed by Ludwieg (1960, 1962, 1964, 1965), assumes that the formation of the internal stagnation point results from the sensitivity of the vortex core to helical, rather than axisymmetric, disturbances. He concludes that the helical mode is the basic mode of breakdown. However, Escudier (1988) points out that experimental evidence suggests that flow upstream of the breakdown is at worst marginally stable. Therefore it does not lend much support to the view that vortex breakdown is

in any sense a direct consequence of instability. This view is supported by the experimental fact that under carefully controlled conditions a purely axisymmetric form of breakdown occurs both in tube-and-vane and closed container experiments. Since it is generally agreed that vortex flows are much more stable to axisymmetric disturbances than to non-symmetric disturbances, the bubble form of breakdown cannot be a direct consequence of instability of the approach flow. Further, breakdown has the appearance of a sudden transition, much like a shock wave or hydraulic jump. There is no evidence of the slow continuous growth typical of hydrodynamic instability.

The abruptness of vortex breakdown suggests the existence of a critical state which separates a supercritical from a subcritical flow state, much like that observed for a hydraulic jump in open channel flows (Benjamin 1962). Leibovich & Randall (1973) point out that the inviscid, linear Squire–Long equation, which is the starting point of Benjamin's work, exhibits a singular behaviour at the critical state, similar to the linearized gasdynamics equation as the Mach number approaches unity. The assumption of small disturbances breaks down for critical flow, and nonlinear effects are required to remove the singular behaviour. Randall & Leibovich (1973) and Leibovich & Kribus (1990) obtain the solitary wave solution at the critical state for the weakly nonlinear and fully nonlinear case, respectively. In order to be able to compare with stationary, i.e. time-independent, experiments exhibiting axisymmetric breakdown, they consider 'trapped' waves, which are defined by zero group velocity. In this way they show that nonlinearity and dispersion balance each other such that the trapped wave of constant form (soliton) yields a streamline pattern that qualitatively resembles the stationary axisymmetric breakdown bubble.

The major difficulty of these wave theories lies in the fact that the subcritical conjugate has a greater momentum flux (flow force) than the supercritical (Benjamin 1962). Since no force is applied to the inviscid flow, Benjamin postulated the existence of a standing train of finite-amplitude waves on the subcritical flow to make up for the difference, caused by a weak vortex breakdown. For stronger transitions he proposed turbulence as the dissipative process in analogy with the theory for the hydraulic jump. Experiments, however, do not support this last view, since strong transitions, involving stagnation of the axial flow, large velocity gradients, and pronounced divergence of streamtubes, can be quite smooth and turbulence free, cf. Escudier (1988). Maxworthy, Hopfinger & Redekopp (1985) point out that if the breakdown bubble is regarded as a manifestation of a finite-amplitude axisymmetric trapped wave followed by a wavetrain, then instability to non-axisymmetric perturbations offers the possibility of large energy transfers from the wave. They conjecture that when the leading wave reaches a certain critical amplitude, the wake-like flow field created by its interior becomes unstable to helical disturbances, a point of view espoused by Escudier *et al.* (1982). Furthermore they point out that often this disturbance grows so rapidly that it completely dominates the flow visualization of the phenomenon, so that usually any sense of an axisymmetric wave is lost, although it still exists in the mean flow and is central to a complete understanding of the whole phenomenon. More detailed theoretical work on primarily flow in pipes has been done by Rusak and his group, cf. Rusak & Judd (2001) and references therein.

Hence, both axisymmetric wave and non-axisymmetric hydrodynamic instability aspects are relevant to the breakdown phenomenon. In an attempt to unify and generalize both concepts, Delbende *et al.* (1998) invoke the concept of local absolute and convective instability (Huerre & Monkewitz 1990) to determine whether the existence of breakdown of a Batchelor vortex (Batchelor 1964) can be correlated

with absolute instability of the flow. They find that the axisymmetric mode never becomes absolutely unstable, implying that the Batchelor vortex never exhibits an axisymmetric breakdown mode. Indeed no results of a Batchelor vortex exhibiting breakdown have been reported in the literature. However, Garg & Leibovich (1979) emphasize that vortex breakdown acts like a solid object in changing an upstream jet-like flow into a wake-like flow. The experimentally observed dominant oscillations of the wake then correspond to the counter-rotating helical mode obtained from the absolute/convective instability analysis for wakes (Delbende *et al.* 1998).

At the same time as the theories discussed above were being developed, significant progress was made towards numerically simulating vortex breakdown. Kopecky & Torrance (1973) and Grabowski & Berger (1976) solve the incompressible steady axisymmetric Navier–Stokes equations for swirling laminar flows in a tube and for trailing wing vortices, respectively. They employ time-independent inflow conditions, raising some concerns (e.g. Leibovich 1978; Spall, Gatski & Grosch 1987), as they artificially constrain the inflow. Such inflow conditions do not allow for upstream propagating disturbances past the inflow plane, which may represent a serious limitation for swirling flows near criticality thresholds. On the other hand, relaxing the fixed inlet boundary conditions may cause the entire breakdown bubble to leave the computational domain.

This issue is addressed independently by Krause (1990) and Spall, Gatski & Ash (1990), who prescribe the axial velocity component on the lateral boundary. Although these authors provide quite different physical justifications and numerical implementations, both sets of simulations successfully model breakdown in tubes, induced and governed by an *a priori* known pressure distribution at the lateral wall. The vortex breakdown remains within the computational domain, which enables the authors to conduct simulations over extended time periods and to study different types of breakdown in radially confined flows, cf. the review articles of Spall & Synder (1999) and Althaus *et al.* (1995*a*). They reproduce the three major types of vortex breakdown observed in tube experiments (e.g. Faler & Leibovich 1977), namely the bubble, helical and double-helical types. Spall & Snyder (1999) and Althaus *et al.* (1995*a*) point out that these different modes are obtained by imposing a fixed inflow swirl ratio and varying the free-stream axial velocity on the lateral boundaries.

In an attempt to circumvent the dependence of the inception and mode selection on the lateral boundary condition, Ruith, Chen & Meiburg (2003) open the radial boundary to mass and momentum flux using a simple radiation boundary condition. Thus, they are able to simulate vortex breakdown in a semi-infinite domain by solving the three-dimensional unsteady Navier–Stokes equations in cylindrical coordinates with a numerical scheme based on that of Verzicco & Orlandi (1996).

The goal of the present direct numerical investigation is to demonstrate that a transition from super- to subcritical as defined by Benjamin (1962) accurately predicts the parameter combination yielding breakdown, if applied locally to a flow with a supercritical inflow profile. Subsequently, we show that the formation of a sufficiently large pocket of absolute instability (Huerre & Monkewitz 1990) in the wake of the axisymmetric breakdown bubble gives rise to a self-excited global mode which governs the breakdown mode selection. Further, by selecting a two-parametric velocity profile for which the steady axisymmetric breakdown is well-studied (Grabowski & Berger 1976), we can address questions regarding the role of three-dimensionality and unsteadiness with respect to the existence, mode selection, and internal structure of vortex breakdown in terms of the two governing parameters and the Reynolds number.

The paper is organized as follows. In § 2 the governing equations in cylindrical coordinates are presented in a format which allows the accurate numerical simulation of the two-parametric velocity profiles (Grabowski & Berger 1976). Section 3 starts with the presentation of a representative case, which subsequently serves as reference case for phenomenological observations as the two governing parameters and the Reynolds number are varied independently. These observations are complemented with mechanistic explanations for the existence and internal structure of breakdown. A more theoretical explanation for the onset of vortex breakdown (Benjamin 1962) is advocated in § 4, while linear global instability as the mechanism of breakdown mode selection is proposed in § 5. Finally, § 6 summarizes the main results.

2. Governing equations and numerical technique

In the present numerical investigation, the incompressible time-dependent three-dimensional Navier–Stokes equations are solved in cylindrical coordinates (r, θ, z). To render the governing equations dimensionless, a characteristic length (L) and velocity (U) are introduced. Their exact form will be discussed below in the context of the specific inflow profile considered in this article. The convective time scale is straightforwardly $T = L/U$ and the characteristic pressure is $P = \rho U^2$, with ρ representing the constant density. Employing the above scaling arguments, the dimensionless continuity equation becomes

$$\frac{\partial q_\theta}{\partial \theta} + \frac{\partial q_r}{\partial r} + r\frac{\partial q_z}{\partial z} = 0, \tag{2.1}$$

while the momentum equations for constant dynamic viscosity μ follow as

$$\left.\begin{aligned}
\frac{\mathrm{D}q_r}{\mathrm{D}t} &= -r\frac{\partial p}{\partial r} + \frac{1}{Re}\left[r\frac{\partial}{\partial r}\left(\frac{1}{r}\frac{\partial q_r}{\partial r}\right) + \frac{1}{r^2}\frac{\partial^2 q_r}{\partial \theta^2} + \frac{\partial^2 q_r}{\partial z^2} - \frac{2}{r}\frac{\partial q_\theta}{\partial \theta}\right], \\
\frac{\mathrm{D}q_\theta}{\mathrm{D}t} &= -\frac{1}{r}\frac{\partial p}{\partial \theta} + \frac{1}{Re}\left[\frac{1}{r}\left(\frac{\partial}{\partial r}r\frac{\partial q_\theta}{\partial r}\right) - \frac{q_\theta}{r^2} + \frac{1}{r^2}\frac{\partial^2 q_\theta}{\partial \theta^2} + \frac{\partial^2 q_\theta}{\partial z^2} + \frac{2}{r^3}\frac{\partial q_r}{\partial \theta}\right], \\
\frac{\mathrm{D}q_z}{\mathrm{D}t} &= -\frac{\partial p}{\partial z} + \frac{1}{Re}\left[\frac{1}{r}\frac{\partial}{\partial r}\left(r\frac{\partial q_z}{\partial r}\right) + \frac{1}{r^2}\frac{\partial^2 q_z}{\partial \theta^2} + \frac{\partial^2 q_z}{\partial z^2}\right].
\end{aligned}\right\} \tag{2.2}$$

Following Verzicco & Orlandi (1996), we write the substantial derivatives in their conservative form

$$\left.\begin{aligned}
\frac{\mathrm{D}q_r}{\mathrm{D}t} &= \frac{\partial q_r}{\partial t} + \frac{\partial}{\partial r}\left(\frac{q_r^2}{r}\right) + \frac{\partial}{\partial \theta}\left(\frac{q_\theta q_r}{r}\right) + \frac{\partial (q_r q_z)}{\partial z} - q_\theta^2, \\
\frac{\mathrm{D}q_\theta}{\mathrm{D}t} &= \frac{\partial q_\theta}{\partial t} + \frac{1}{r^2}\frac{\partial (r q_\theta q_r)}{\partial r} + \frac{1}{r}\frac{\partial q_\theta^2}{\partial \theta} + \frac{\partial (q_\theta q_z)}{\partial z}, \\
\frac{\mathrm{D}q_z}{\mathrm{D}t} &= \frac{\partial q_z}{\partial t} + \frac{1}{r}\frac{\partial (q_r q_z)}{\partial r} + \frac{1}{r}\frac{\partial (q_\theta q_z)}{\partial \theta} + \frac{\partial q_z^2}{\partial z}.
\end{aligned}\right\} \tag{2.3}$$

Following Verzicco & Orlandi (1996) we assume $q_r = v_r r$, $q_\theta = v_\theta$, and $q_z = v_z$, where v_r, v_θ, v_z are the velocity components in the radial, azimuthal and axial directions, respectively. The variables t and p represent time and pressure, respectively, while the

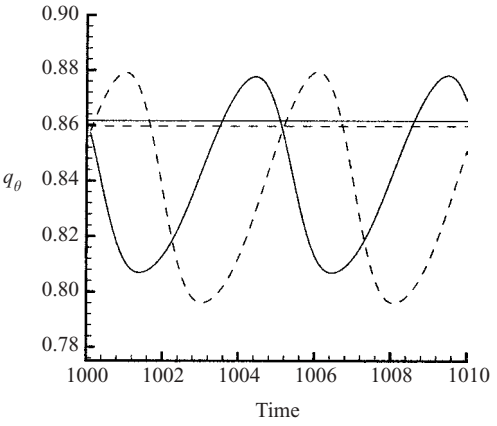

FIGURE 1. Azimuthal velocity component q_θ of the reference (solid line) and higher-resolution case (dashed line) over time. The constant horizontal lines, corresponding to axisymmetric calculations, reveal a marginal difference of about 0.2%. The oscillatory behaviour of the three-dimensional simulations exhibits no detectable difference in the period; however the maxima and minima differ by 0.2% and 1.4%, respectively.

Reynolds number is defined as

$$Re = \frac{UL}{\nu}. \tag{2.4}$$

The governing equations are solved in primitive variables by a numerical scheme based on that of Verzicco & Orlandi (1996). The spatial discretization on a staggered grid employs a finite-difference scheme, with second-order spatial accuracy everywhere, including the axis. Then the geometrical singularities at the axis of the form r^{-1}, r^{-2}, r^{-3} only are apparent since only q_r has to be evaluated there and $q_r(r=0)=0$, by definition. Consequently the other velocity components do not have to be redefined. The solution is advanced in time by a fractional-step method employing an approximate-factorization technique. The time step employed is typically $\Delta t = 0.025$.

We employ the radial coordinate transformation of Grabowski & Berger (1976) that concentrates grid points in the region near the axis. In contrast the grid points are equidistant in the azimuthal and axial directions. The computational domain has the dimensions $R_d = 10$ and $Z_d = 20$, which has been shown to be sufficient (Ruith *et al.* 2003). Unless mentioned otherwise it is resolved by $n_r = 61$, $n_z = 193$ and $n_\theta = 61$ grid points in the radial, axial and azimuthal directions, where the latter applies only to the non-axisymmetric simulations. The numerical scheme is accelerated by parallelizing the code with MPI. The reference case discussed above takes about 40 hours on 12 processors of an SGI Origin 3400 to reach $t = 2000$.

The grid independence has been checked by comparing the reference case (solid lines) with a high-resolution simulation (dashed lines) employing $n_r = 97$, $n_z = 241$ and $n_\theta = 97$ grid points, see figure 1, for the example q_θ at $z = 5$ and $r = 1$. The constant horizontal lines, corresponding to axisymmetric calculations, reveal a marginal difference of about 0.2% from the high-resolution case. The oscillatory behaviour of the three-dimensional simulations exhibits no detectable difference in the period; however the maxima and minima differ by 0.2% and 1.4%, respectively. The phase shift between the computations is caused by grid-dependent round-off errors

feeding on a physical instability, which ultimately yields the oscillatory behaviour of the flow field.

2.1. *Boundary conditions*

As mentioned above, the characteristic scales depend on the inflow velocity profile. In the present article we will discuss low entrainment velocity profiles, which have been explored by Grabowski & Berger (1976) for the steady axisymmetric case. This provides an opportunity to investigate the spatio-temporal evolution as well as three-dimensional effects for this class of flows, referred to as 'Grabowski profiles' hereafter. Note that the velocity profile at the inflow boundary is kept axisymmetric and constant over time, and no perturbations are superimposed.

The use of such steady inflow conditions has been criticized in the context of simulating trailing wing vortices (e.g. Leibovich 1978; Spall *et al.* 1987) as they do not allow the upstream propagation of disturbances past the inflow plane. However, recent numerical simulations of breakdown in a full tube-and-vane apparatus, as well as with fixed supercritical (see § 4) inflow conditions derived from the results using the complete vane geometry (Snyder & Spall 2000) demonstrate that breakdown location and structure are essentially unaffected by the use of this approximation.

Thus, in their case, upstream-propagating non-axisymmetric disturbances close to the inflow boundary do not exist or have negligible effects on the vortex breakdown, and it is unnecessary to design inflow boundary conditions that appear transparent to these perturbations. This suggests that our choice of fixed, steady inflow boundary conditions will not unduly constrain the development of the various vortex breakdown modes further downstream as long as supercritical inflow conditions are assumed. However, as will be discussed in the following sections, results employing subcritical inflow conditions (§ 4) have to be interpreted with some care. Nevertheless such results are of physical significance, since such flows can be a result of the geometry upstream of the inflow, e.g. a nozzle.

Grabowski profiles exhibit a vanishing radial velocity component, while the axial and azimuthal components are defined piecewise for the regions inside and outside a characteristic radius R, respectively. The axial velocity component can exhibit a jet-like or wake-like character inside R, and reaches a constant free-stream velocity $\tilde{v}_{z,\infty}$ outside R. The non-dimensional form of the velocity profile is obtained by scaling the radius with the characteristic core radius $L = R$, and the velocities with the free-stream axial velocity $U = \tilde{v}_{z,\infty}$. The two-parameter non-dimensional velocity components then take the form

$$\left.\begin{aligned} v_\theta(0 \leqslant r \leqslant 1) &= Sr(2 - r^2), \\ v_\theta(1 \leqslant r) &= S/r, \\ v_r(r) &= 0, \\ v_z(0 \leqslant r \leqslant 1) &= \alpha + (1 - \alpha)r^2(6 - 8r + 3r^2), \\ v_z(1 \leqslant r) &= 1, \end{aligned}\right\} \tag{2.5}$$

Here the swirl parameter S represents the azimuthal velocity at the edge of the core relative to the axial free-stream velocity, $S = \tilde{v}_\theta(R)/\tilde{v}_{z,\infty}$. The coflow parameter α denotes the ratio of the axial velocity at the axis to the axial free-stream velocity, $\alpha = \tilde{v}_{z,c}/\tilde{v}_{z,\infty}$. Setting α greater or less than one yields a jet-like or wake-like behaviour, respectively. The properties of the Grabowski profile are sketched in figure 2.

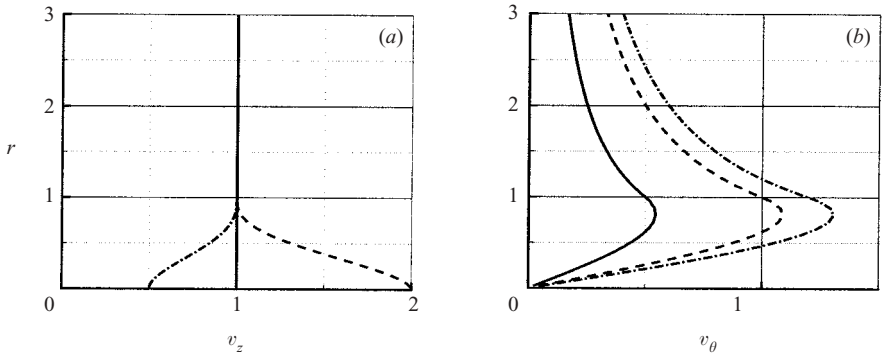

FIGURE 2. (*a*) Axial velocity distribution for the Grabowski profiles: solid line $\alpha = 1.0$, dashed line $\alpha = 2.0$, dash-dot line $\alpha = 0.5$. (*b*) Azimuthal velocity distribution: solid line $S = 0.5$, dashed line $S = 1.0$, dash-dot line $S = 1.2$.

To enable the simulation of spatially and temporally evolving swirling jets, the outflow and lateral boundaries employ simple radiation conditions of the form

$$\frac{\partial q_i}{\partial t} + C\frac{\partial q_i}{\partial z} = 0, \qquad \frac{\partial q_i}{\partial t} + C_r\frac{\partial q_i}{\partial r} = 0, \tag{2.6}$$

respectively. Allowing mass and momentum flux through the radial boundary permits the use of relatively small radial domain sizes without artificially confining the flow, cf. Ruith *et al.* (2003). Despite the additional mass exchange over the radial boundary, these authors show that the flow field thus obtained is solenoidal to within machine accuracy for arbitrary times, if the convection velocities C and C_r are assumed to be constant. The exact values of C and C_r have been shown not to be critical to the solution.

In contrast to the present simulation Grabowski & Berger (1976) employ homogeneous Neumann conditions for all velocity components at the outflow and $\partial q_r/\partial r = 0$, $q_\theta = S/r$ and $q_z = 1$ (type 2 in Ruith *et al.* 2003) at the radial boundary. Nevertheless the results agree well as will be discussed below. For further details concerning the numerical technique and boundary conditions, as well as for additional validation results, the interested reader is referred to Ruith *et al.* (2003).

3. Phenomenological observations and mechanistic explanations

In the following we will commence by describing the temporal and spatial evolution of a typical flow, which can subsequently serve as a reference case when discussing the effects of the variations in the individual parameters. First, simulation results will be presented that serve to identify the dominant mechanisms in qualitative terms. Subsequently, several quantitative measures of the flow evolution will be introduced, and their dependence on the values of the governing parameters will be discussed.

3.1. *Reference case*

As a representative reference case, a swirling jet is selected for which the dimensionless physical parameters take the values $Re = 200$, $\alpha = 1$, and $S = 1.095$. It is identical with the reference case discussed in § 2.

In order to be able to compare with the results of Grabowski & Berger (1976), an axisymmetric calculation ($\partial/\partial\theta = 0$) is carried out in addition to the fully

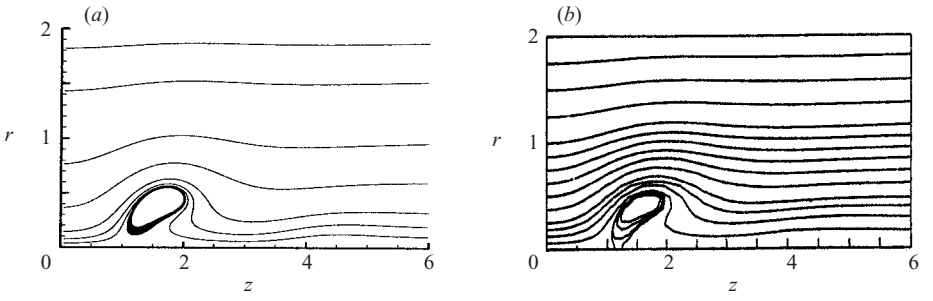

FIGURE 3. Reference case: $Re = 200$, $\alpha = 1$, and $S = 1.095$. Projected streamlines in the meridional plane obtained for the axisymmetric steady state (*a*) compared with the original streamlines obtained by Grabowski & Berger (1976) (*b*) (reprinted with the permission of Cambridge University Press). Despite the lower spatial resolution in the original simulation, the agreement is good.

three-dimensional one. Figure 3 shows streamlines projected in the meridional plane of the current axisymmetric steady-state result (frame *a*), as well as the original axisymmetric and steady result of Grabowski & Berger (frame *b*). Here, the steady state is defined by requiring that the velocity components change by less than 10^{-12} over $\Delta t = 10$. We find that despite the lower spatial resolution employed by Grabowski & Berger, the projected streamlines agree very well.

Figure 4 shows a streakline visualization of the three-dimensional reference case at three subsequent times $t = 400$, $t = 600$ and $t = 900$, respectively. The streaklines are obtained by releasing particles at six equidistant azimuthal positions close to the axis ($r = 0.05$) at the left (inflow) boundary. The columnar initial condition ($q_r = 0$ and $\partial/\partial z = 0$), which prescribes the invariant inflow Grabowski profile at all axial positions, evolves toward an axisymmetric bubble breakdown state. It reaches a quasi-steady state around $t = 400$ which is equivalent to the steady-state solution obtained for the axisymmetric simulation presented in figure 3. For the parameter combination under consideration the axisymmetric breakdown state becomes unstable to helical disturbances in the wake of the bubble ($t = 600$). The disturbances travel upstream into the bubble, causing a transition which finally settles into a helical breakdown mode around $t = 900$. Although the results presented start from an initially columnar vortex, the same transition is observed if we take an axisymmetric steady-state result as initial condition.

3.1.1. *Vorticity considerations*

Vortex breakdown is only observed for highly swirling flows. Traditionally an angle of swirl ϕ is defined by $\phi = \arctan(v_\theta/v_z)$ and, as a rule of thumb, it is found that the maximum value of ϕ upstream of breakdown is larger than about 40°, cf. Hall (1972). Clearly, the vortex breakdown phenomenon is too complex to be captured accurately by this criterion, since it depends strongly on the interplay among the velocity, vorticity and pressure fields.

Nevertheless, the high maximum swirl angle $\phi = 50°$ of the reference case indicates a highly concentrated vortex core, with the dimensionless pressure p at the centre $r = 0$ being much lower than the ambient pressure. Since the axisymmetric columnar initial condition satisfies the steady Euler equations, viscous diffusion of axial vorticity away from the axis starts the evolution of the flow. This effectively reduces the induced velocity near the vortex axis, thereby increasing p locally. Adverse pressure gradient

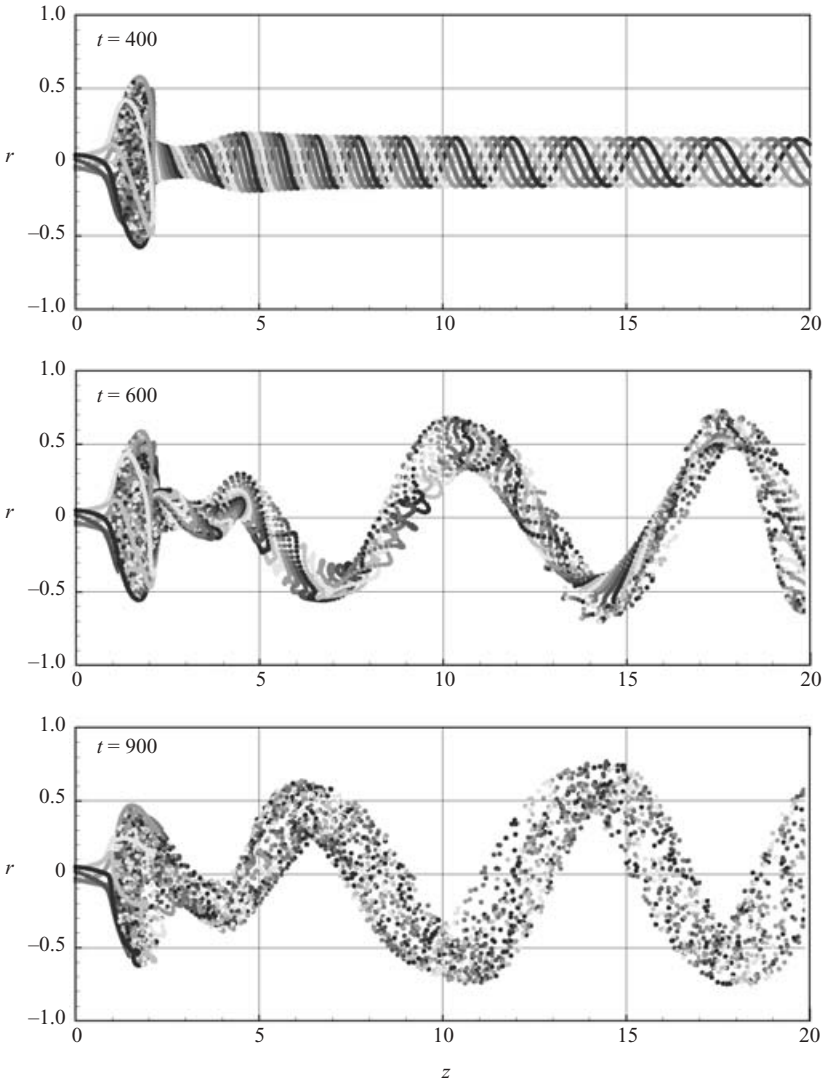

FIGURE 4. Reference case: visualization of flow field with streaklines consisting of particles released at the inflow (left) boundary close to the axis. Starting from a columnar vortex a quasi-steady state is reached at time $t = 400$. It becomes unstable to helical disturbances in the wake of the bubble ($t = 600$) and is consequently superseded by a helical breakdown mode ($t = 900$).

and viscous diffusion yield a divergent vortex core, setting off a physical feedback mechanism that ultimately leads to vortex breakdown (Brown & Lopez 1990).

This mechanism is illustrated in figure 5 for the axisymmetric reference case. This, however does not constitute a limitation, since it is found that three-dimensional disturbances become relevant only later in the temporal evolution. The columnar vortex at $t = 0$ (not shown here) exhibits no azimuthal vorticity, since $\alpha = 1$; however by $t = 2$ negative azimuthal vorticity ω_θ together with a slight divergence of the streamlines becomes visible. Along the diverging core, downstream portions of a vortex line are at greater radial locations than upstream portions. Conservation of

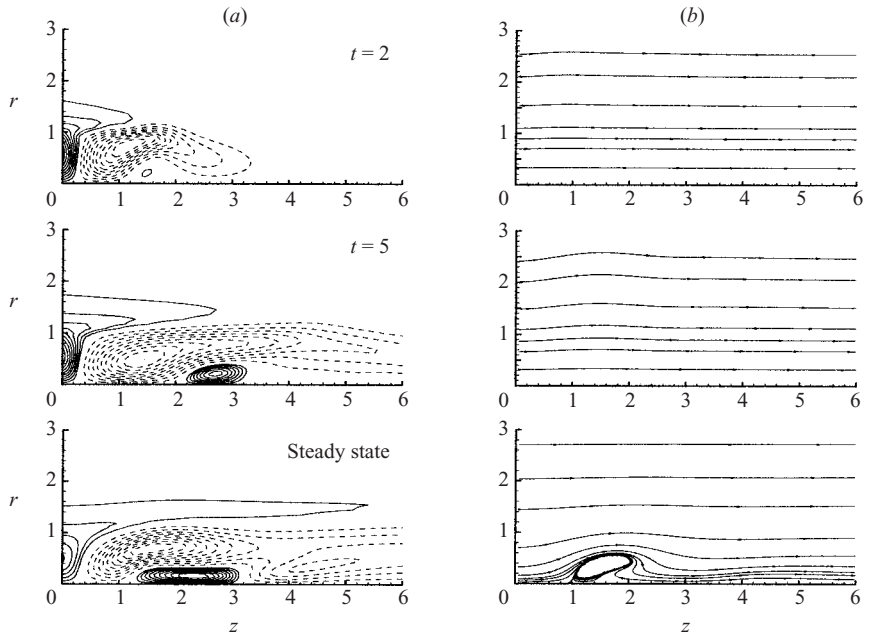

FIGURE 5. Reference case: temporal evolution of the normalized azimuthal vorticity ω_θ (*a*) together with the projected streamlines (*b*) assuming axisymmetry. ω_θ is normalized with the maximum positive and minimum negative level for positive and negative contours, respectively. The displayed increments are $\Delta\omega_\theta = 0.1$. Similar to the swirling pipe flow results of Brown & Lopez (1990) the generation of negative vorticity (dashed lines) precedes the formation of a free stagnation point, i.e. vortex breakdown.

azimuthal momentum requires then that fluid particles at large radii rotate more slowly, thus tilting the vortex line into a spiralling helix. The winding sense of the helix can be deduced from figure 6(*a*), assuming a mathematically positive azimuthal velocity component and considering a view from above, looking upstream such that the shaded areas are behind the vortex. Then the vortex lines wind in the opposite direction to the ambient velocity. The produced azimuthal vorticity component is negative and thus induces an upstream-directed component of axial velocity which decelerates the flow. By continuity the core expands further, which in turn produces additional negative azimuthal vorticity which perpetuates the cycle and establishes the feedback loop. Hence the temporal evolution observed in the present semi-infinite domain is similar to the swirling pipe flow results of Brown & Lopez (1990).

The reference case becomes ultimately unstable to azimuthal disturbances which leads to wave-like behaviour in the wake of the bubble. The emerging helical breakdown structure is seen in the vortex lines plotted in figure 6(*b*) which compare qualitatively with the numerical results of Saghbini & Ghoniem (1997) obtained by a vortex filament simulation.

3.1.2. *Pressure and velocity considerations*

In this subsection it is demonstrated that the breakdown phenomenon under consideration does not require any pressure gradient in the far field, although it exhibits a strong adverse pressure gradient in the vortex core, cf. figure 7(*a*) taken from the axisymmetric reference case at steady state. Consequently, the axial velocity v_z (figure 7*b*) is decelerated, and it ultimately reaches negative values for the considered

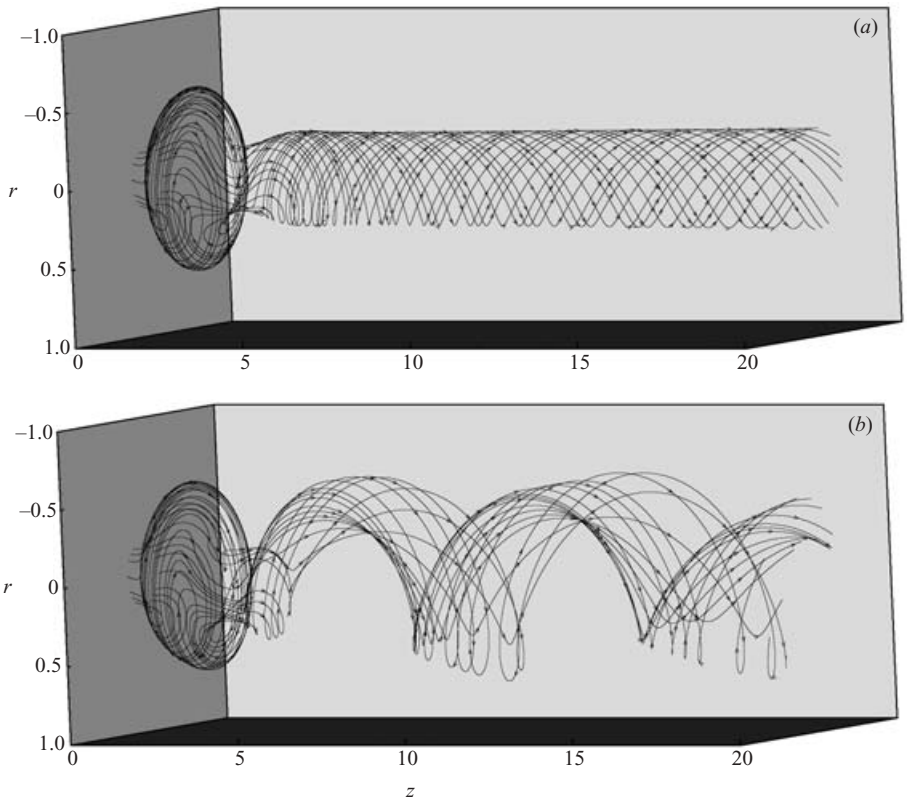

FIGURE 6. Reference case: vorticity lines at time (*a*) $t = 400$ and (*b*) 1000. Similar to the streaklines, vorticity lines reveal an axisymmetric bubble breakdown at $t = 400$ which eventually becomes unstable toward azimuthal disturbances und ultimately settles into a helical breakdown mode ($t = 1000$).

case. Two free internal stagnation points forming a closed region of reversed axial flow are obtained. To satisfy mass conservation, radial outflow is required upstream of the recirculation region (figure 7*c*) which is succeeded by radial inflow in the wake of the bubble. However, the latter is smaller in magnitude, leaving a less concentrated vortex core in the wake. The azimuthal velocity component v_θ almost vanishes inside the bubble, shifting fluid particles carrying azimuthal momentum to larger radii. To conserve azimuthal momentum, the magnitude of v_θ has to decrease, cf. figure 7(*d*). In the wake of the bubble a secondary swelling is formed causing similar, though less pronounced, behaviour in the pressure and velocity fields.

In contrast, the far field ($r = 8$) does not exhibit an axial gradient of the pressure (or any of the velocity components). As has been demonstrated in many experiments on delta wings and tubes (cf. e.g. the review article by Lucca-Negro & O'Doherty 2001), imposed axial pressure gradients in the far field have profound effects on vortex breakdown. Thus, in some sense, the axial pressure gradient in swirling flows consists of two components: the imposed external pressure gradient and the contribution due to the swirl. Lucca-Negro & O'Doherty point out that under certain circumstances a positive axial pressure gradient can exist on the axis even if the imposed pressure gradient is negative. The above-mentioned 'decomposition' of the pressure field has been independently employed by Krause (1990) and Spall *et al.* (1990) in

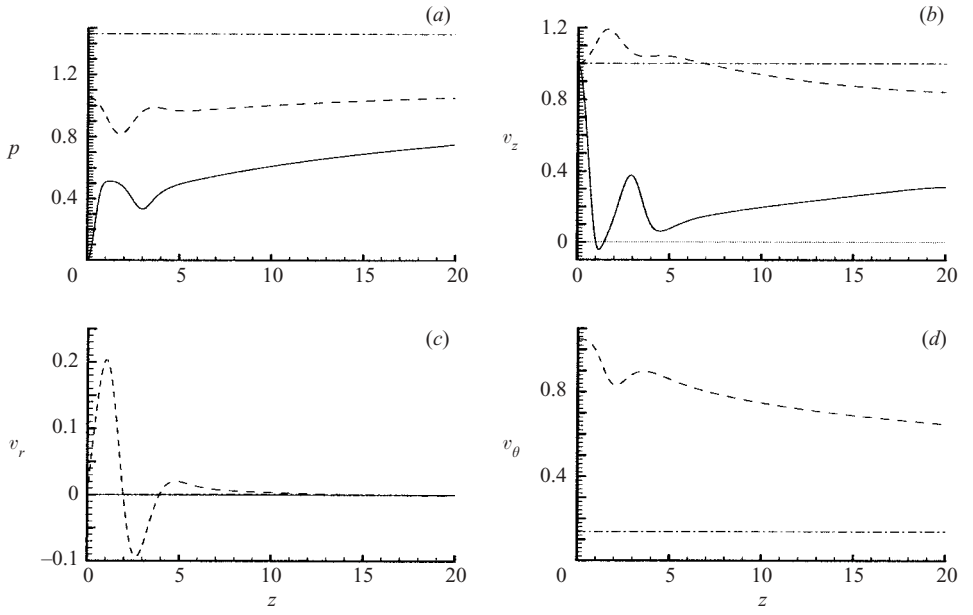

FIGURE 7. Reference case: pressure (*a*), axial (*b*), radial (*c*), and azimuthal velocity component (*d*) at different radial positions (solid line: $r = 0$, dashed line: $r = 1$, and dash-dotted line: $r = 8$) as a function of the axial position. The values taken represent the axisymmetric steady state of the reference case. Breakdown on the axis, exhibiting two internal stagnation points with a recirculation zone in between, is confirmed in the v_z plot. It corresponds to a sharp increase in core pressure and radial outflow, while v_θ has to decrease to conserve azimuthal momentum.

three-dimensional numerical simulations of vortex breakdown. By prescribing a far-field pressure gradient on the lateral boundary of their computational domain they successfully initiate vortex breakdown and are further able to govern its mode selection, cf. the review articles by Althaus *et al.* (1995*a*) and Spall & Snyder (1999). This is typically done by prescribing the axial velocity on the lateral boundary with variations along the axis of the same order as in the jet centre, see for example Breuer & Hänel (1993).

The three-dimensional evolution of the reference case is illustrated in figure 8 by the pressure distribution in a meridional slice for two times $t = 400$ and 1000. At both times a sharp pressure increase is observed upstream of the internal stagnation point. In the wake of the bubble structure a local pressure minimum forms. A swelling of the axisymmetric streaklines at $t = 400$ originates at the downstream end of this minimum. At the later time $t = 1000$ we confirm that the particles forming the helix are concentrated in the low-pressure regions. However no local pressure minimum can be observed at the location of the helix. Therefore pressure isosurfaces are inappropriate means to visualize the structure of breakdown, cf. also Jeong & Hussain (1995).

3.2. *Influence of swirl parameter S*

It is instructive to compare the above reference case to simulations which only differ in the applied swirl S. Therefore the other parameters take the same values as before, i.e. $Re = 200$, $\alpha = 1$. For swirl levels below the critical value $S_c = 0.8944$, no internal stagnation point forms and the vortex does not break down (not shown here). Further, for the low Reynolds number employed, no amplified helical instabilities are observed until the simulation is stopped at $t = 2000$.

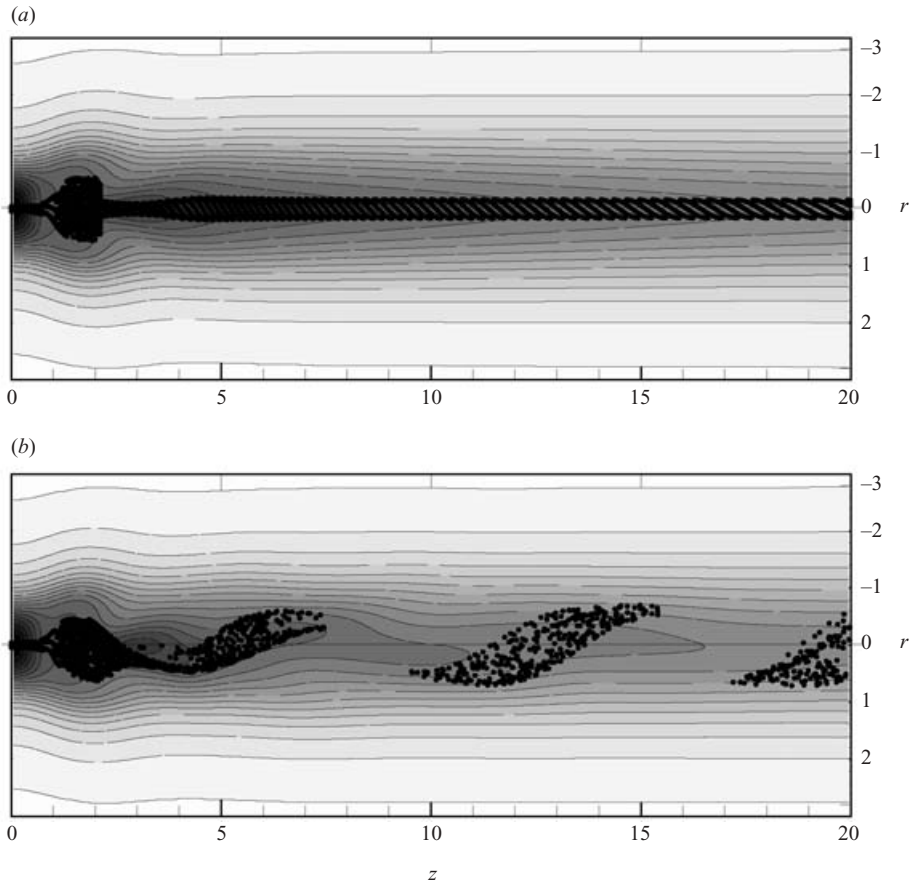

FIGURE 8. Reference case: meridional slice of normalized pressure contours with superimposed streaklines at time (*a*) $t = 400$ and (*b*) 1000. The pressure is normalized with the maximum, and levels are distributed equally with $\Delta p = 0.05$ between low pressure (dark areas) and high pressure (light areas). A sharp increase in pressure upstream of the stagnation point is followed by a local pressure minimum in the wake of the bubble.

Figure 9 (top frame) displays the streaklines for the incipient breakdown state $S = S_c = 0.8944$ for which a free stagnation point first exists. Thus S_c observed for the present time-dependent three-dimensional simulation coincides with $S = 0.8944$ for which Grabowski & Berger (1976) first observed a 'well pronounced bulge' and an internal stagnation point for their steady axisymmetric simulation. The incipient bubble breakdown remains stable to azimuthal disturbances and thus axisymmetric. On increasing the swirl to slightly higher values, a temporal evolution similar to the reference case is seen. The columnar initial condition evolves toward a quasi-steady axisymmetric bubble breakdown state which ultimately becomes unstable to three-dimensional disturbances. This is demonstrated in figure 10, which tracks the maximum velocity flux change q_{max} between time increments $\Delta t = 0.5$. All cases considered exhibit a pronounced local minimum of q_{max}, indicating the quasi-steady state, which for sufficiently high S is superseded by a periodic behaviour for which q_{max} levels out at high values. In what follows below, we will discuss the different helical breakdown modes into which the flow finally settles.

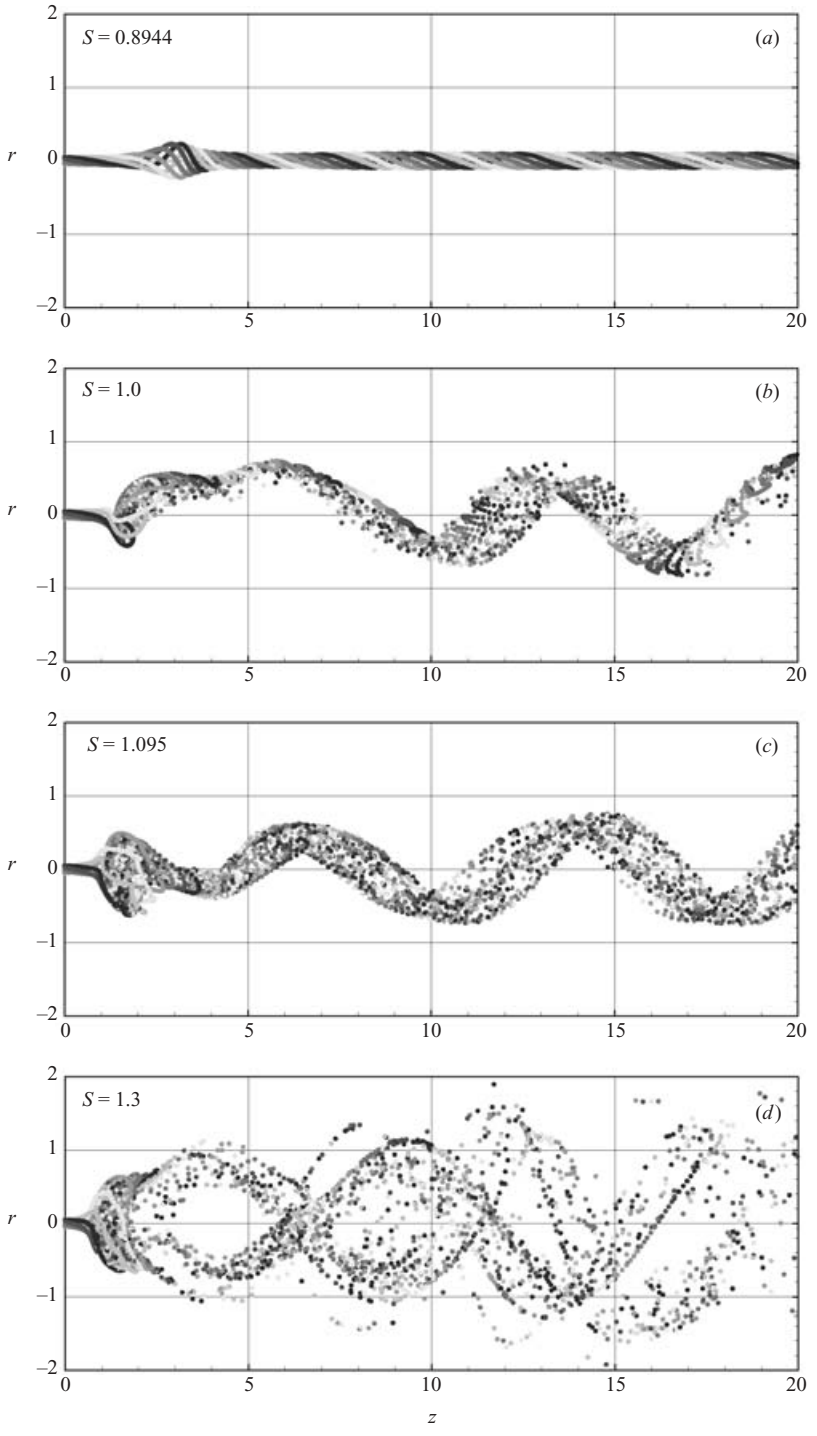

FIGURE 9. $Re = 200$, $\alpha = 1$, and $S = 0.8944$, 1.0, 1.095, 1.3: a snapshot of the streaklines at time $t = 1850$. The lowest-swirl case ($S = 0.8944$) remains axisymmetric and forms a steady bubble breakdown, while the higher swirl employed in the other examples renders the quasi-steady axisymmetric bubble breakdown helically unstable. Ultimately they settle into a helical or double-helical breakdown mode for lower respectively higher S.

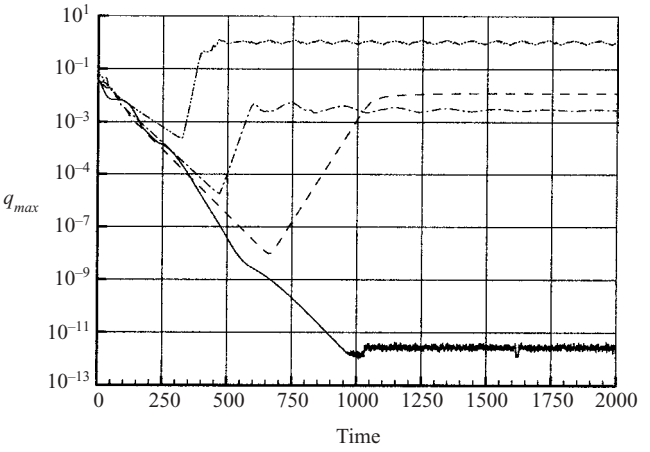

FIGURE 10. $Re = 200$, $\alpha = 1$, at $S = 0.8944$ (solid line), $S = 1.0$ (dashed line), $S = 1.095$ (dash-dotted line) and $S = 1.3$ (dash-dot-dotted line). Temporal evolution of the three-dimensional simulation for different swirl parameters in terms of maximal velocity flux change q_{max} per time increment $\Delta t = 0.5$. The case $S = 0.8944$ reaches an axisymmetric steady state, while a higher swirl parameter ($S = 1.0$, $S = 1.095$, and $S = 1.3$) renders the flow three-dimensional, after reaching an axisymmetric, quasi-steady state.

The lowest swirl considered in this regard $S = 1.0$ (figure 9*b*) exhibits a helical mode similar to the reference case (figure 9*c*). However for this lower S the bubble is smaller and located at a slightly more downstream position. The highest swirl considered here employs the parameter $S = 1.3$ (figure 9*d*) which replaces the single helix observed before with a 'pulsant' double-helical breakdown mode.

By 'pulsant' we refer to the varicose pulsating bubble which is 'emptied' at the downstream end with a period of about $T = 105$ non-dimensional time units, cf. figure 11. After the bubble is emptied, thereby reducing its size, its downstream end closes and it starts to grow until it bursts again, releasing particles on a rotating, double-helical path. The interested reader is referred to the online version of Ruith & Meiburg (2002*a*) for a temporal animation of this phenomenon. Note that this axisymmetric 'unsteadiness' on the longer time scale is not observed for the lower swirl numbers discussed above. For the given parameter combination it is a three-dimensional effect, which is not observed in axisymmetric simulations. However, as will be shown in § 3.4, higher Reynolds numbers potentially yield axisymmetric pulsating bubbles.

Above we based the classification of the breakdown mode observed on visualizations by streaklines much as done in physical experiments. However, vortex breakdown can be regarded as perhaps the most visible and stable coherent structure (CS) in fluid mechanics (Garg & Leibovich 1979). Therefore, it is illuminating to determine the vortex breakdown structure by criteria developed for the appropriate definition and identification of a vortex CS in other classes of flows.

This question was already touched upon in figure 8. Although particles tend to be concentrated in low-pressure regions, no local pressure minima form, making pressure isosurfaces inappropriate means to visualize the structure of breakdown. On the other hand Jeong & Hussain (1995) demonstrate that a local pressure minimum can be a consequence of unsteady strain (not a CS), leading them to the conclusion that the existence of a local pressure minimum is neither a sufficient nor a necessary condition for the presence of a vortex core in general.

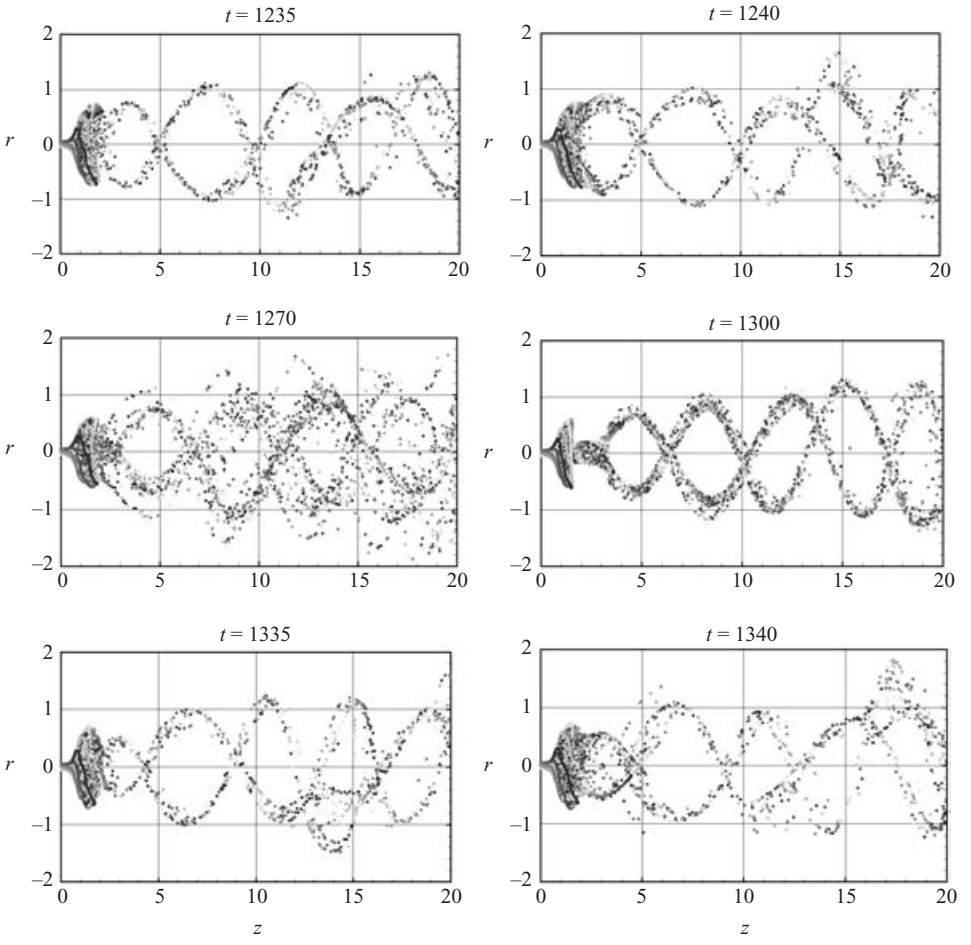

FIGURE 11. $Re = 200$, $\alpha = 1$, and $S = 1.3$. For this comparably large S a varicose pulsating bubble exists which is 'emptied' at the downstream end with a period of about $T = 105$ non-dimensional time units. The released particles follow a rotating double-helical path.

Another widely used criterion to educe vortex cores (Hussain & Hayakawa 1987; Bisset, Antonia & Browne 1990, etc.) employs the vorticity magnitude $|\omega| = \sqrt{\omega_r^2 + \omega_\theta^2 + \omega_z^2}$. Considering several examples, Jeong & Hussain (1995) conclude that a $|\omega|$ surface at a sufficiently low level is a necessary but not sufficient condition to detect a tubular vortex CS, since background shear might lead to vorticity sheets exhibiting large vorticity magnitudes without being a vortex core. It is especially problematic and sometimes impossible to determine the appropriate $|\omega|$ threshold that simultaneously displays vortices with a large variation in $|\omega|$.

In an attempt to define a necessary and sufficient condition for the existence of a vortex in an incompressible flow, Jeong & Hussain (1995) suggest a criterion which has as its starting point the existence of a pressure minimum. However, they discard the two effects which they identified to be responsible for the inconsistency between the existence of a pressure minimum and the existence of a vortex core: (i) unsteady straining, which can create a pressure minimum without involving a vortical motion, and (ii) viscous effects, which can eliminate the pressure minimum in a flow with vortical motion. This yields the definition of a vortex core as a connected region with

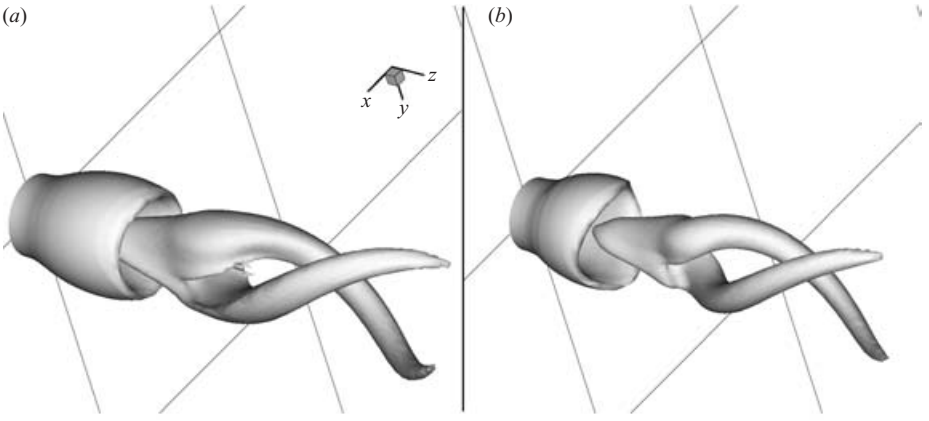

FIGURE 12. $Re = 200$, $\alpha = 1$, and $S = 1.3$. (*a*) The vorticity iso-surface $|\omega| = 0.4$ and (*b*) the λ_2 iso-surface $\lambda_2 = -0.2$ (Jeong & Hussain 1995) confirm the double-helical structure of vortex breakdown suggested by the streakline visualization shown above. However, the azimuthal mode-two deformation of the pulsating bubble is only seen in the λ_2 iso-surface. The displayed case corresponds to a time $t = 1000$ and the distance between grid lines displayed is $\Delta = 5$.

two negative eigenvalues of the symmetric tensor $\mathcal{S}^2 + \Omega^2$. Here $\mathcal{S}$ and Ω are the symmetric and antisymmetric part of the velocity gradient tensor ∇v, respectively. Ordering the three real eigenvalues λ in a sequence such that $\lambda_1 \geqslant \lambda_2 \geqslant \lambda_3$, the definition is equivalent to the requirement that $\lambda_2 < 0$ within the vortex core, which gave the criterion its popular name: λ_2-criterion.

Figure 12 compares the vortical structures of the case employing $S = 1.3$ obtained with the $|\omega|$-criterion (frame *a*) and λ_2-criterion (frame *b*). In the $|\omega|$ case we normalized with the maximal (positive) vorticity magnitude, while the minimal (negative) value of λ_2 is used as reference value for the λ_2-criterion. The structures revealed by $|\omega| = 0.4$ and $\lambda_2 = -0.2$ are very similar. Both criteria capture the double-helical tail of the vortex breakdown, in agreement with the streakline visualizations. However, the azimuthal mode-two deformation of the pulsating bubble is only seen in the λ_2 iso-surface. Further, in contrast to the λ_2-criterion, the selection of the appropriate threshold value using the $|\omega|$-criterion is critical in order to not hide the double-helical structure.

3.2.1. *Internal structure of the breakdown bubble*

A question of prime importance in combustion and mixing applications pertains to the internal structure of the breakdown bubble. Early investigations in guide-vane experiments with diverging tubes (Sarpkaya 1971*a*) reveal a *one-celled* structure with a vortex ring at the downstream end of the bubble. If the axisymmetric bubble evolves from an axisymmetric swelling of the vortex core, it encloses an ovoid region of circulating fluid, in agreement with the present numerical investigation. The initiation of vortex breakdown by an axisymmetric swelling has further been experimentally confirmed by Escudier (1988), as well as by Althaus *et al.* (1995*a*, *b*) both experimentally and numerically. If the axisymmetric bubble breakdown evolves from either a single helix or a double helix, the observed vortex ring gyrates around the centreline and seems to fill the bubble from its downstream end, whereas it empties it from its upstream part. This mechanism of mass exchange is confirmed by Brücker

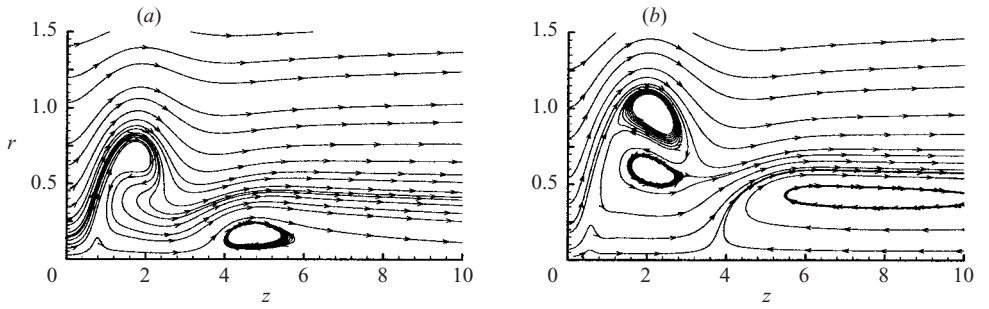

FIGURE 13. $Re = 200$, $\alpha = 1$, $S = 1.3$ (*a*), and $S = 1.6$ (*b*). Both one-celled ($S = 1.3$) and two-celled ($S = 1.6$) axisymmetric steady-state bubble structures are observed depending on the swirl parameter S. Thus the fixed inflow conditions do not prevent the existence of two-celled structures. Note that both cases exhibit a multiple bubble breakdown, visible as a second, corotating bubble further downstream. These results are obtained from axisymmetric simulations.

& Althaus (1992), who use a cylindrical tube with a converging–diverging insert in an apparatus that is otherwise similar to the one employed by Sarpkaya.

In contrast, the guide-vane experiments with diverging tubes of Faler & Leibovich (1978) reveal a *two-celled* structure with a counter-rotating vortex ring inside the breakdown bubble. In this topology, the mass exchange at the rear of the bubble is explained as follows: one ring fills the bubble, whereas the other, counter-rotating vortex ring empties it.

Similarly to the physical experiments discussed above, numerical experiments reveal both one-celled (Grabowski & Berger 1976) and two-celled (Spall *et al.* 1990; Breuer & Hänel 1993) morphologies. Axisymmetric simulations, cf. figure 13, confirm the existence of both one- and two-celled structures at steady state. Here the swirl number $S = 1.3$ exhibits a one-celled structure, while increasing the swirl parameter to $S = 1.6$ gives rise to a two-celled bubble structure. The latter is similar to the numerical simulation data of Breuer & Hänel (1993) and Spall *et al.* (1990), and thus indicates that the fixed inflow conditions employed in the present investigation do not prevent the existence of two-celled structures. However these experiments have to be interpreted with some caution, in particular in the vicinity of the inlet since the inflow is subcritical (§ 4) and part of the upstream influence might enter, in conflict with the fixed inflow boundary conditions. Similar problems occur in physical experiments. Note that the one- and two-celled internal structure of the bubble, where the latter exhibits a counter-rotating vortex, is not to be confused with a multiple bubble breakdown structure. The latter exhibits corotating vortices, substantially separated in the axial direction, see § 3.4 for further details.

We suspect that the existence of the two-celled bubble structure is a result of a local centrifugal instability (Rayleigh 1917), since it has been shown that swirl modifies jet flows dominated by a Kelvin–Helmholtz instability where only corotating vortices are possible, in that it results in the formation of counter-rotating vortex structures, cf. Martin & Meiburg (1994). Here a parameter Rc is defined as $Rc = \mathrm{d}\Gamma_z^2/\mathrm{d}r$, where Γ_z represents the axial circulation. Then the classic Rayleigh criterion states that a necessary and sufficient condition for linear stability to axisymmetric disturbances $m = 0$ of a steady inviscid purely swirling flow is that $Rc \geqslant 0$. Clearly, the presence of an axial velocity component, viscosity, etc. modifies this condition; however, as discussed below, we find that it is still a useful diagnostic.

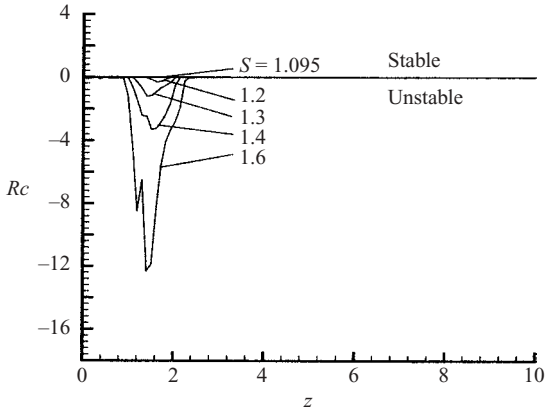

FIGURE 14. Centrifugal instability as defined by Rayleigh (1917) for purely swirling inviscid flow applied to the present axisymmetric steady simulation results employing $Re = 200$, $\alpha = 1.0$ and increasing S. Larger swirl values S cause stronger centrifugal instability that can ultimately lead to a counter-rotating vortex ring, i.e. to a two-celled internal bubble structure.

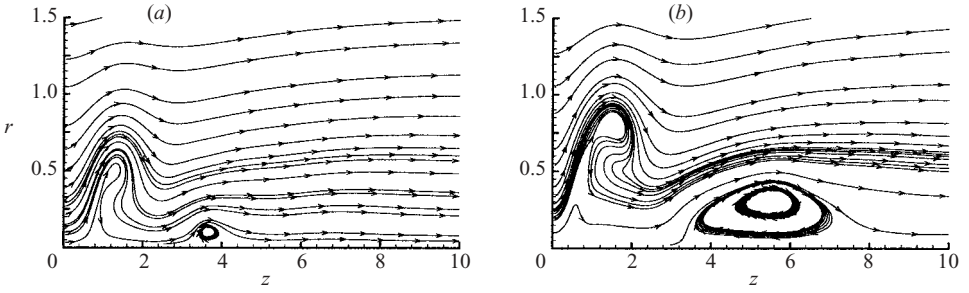

FIGURE 15. $Re = 200$, $\alpha = 1$, $S = 1.3$ (a), and $S = 1.6$ (b). In contrast to figure 13 the streamlines obtained by azimuthal averaging of a three-dimensional calculation at $t = 1000$ are plotted, which exhibit a one-celled structure for both cases.

Figure 14 shows the tendency toward centrifugal instability as defined by Rayleigh (1917) for the present axisymmetric steady simulation results employing $Re = 200$, $\alpha = 1.0$ and increasing S. This corresponds to a physical experiment in which the swirl parameter is slowly increased in time and Rc is recorded to determine the tendency toward the formation of counter-rotating vortices. Larger swirl values S decrease Rc and ultimately lead to a counter-rotating vortex ring, i.e. to a two-celled internal bubble structure as seen in figure 13.

Finally we wish to address the important question of whether the axisymmetric results presented above predict averaged three-dimensional simulation results. For this reason we compute the azimuthally averaged velocity at a time $t = 1000$ for which the reference case and cases employing higher S exhibit a helical breakdown mode. No significant differences are seen for the reference case (not shown here); however as the swirl parameter is increased further, significant deviations become apparent.

Figure 15 illustrates the azimuthally averaged streamlines for the cases $S = 1.3$ and $S = 1.6$, whose axisymmetric properties have been discussed earlier in figure 13. Here, the breakdown bubbles appear smaller, and $S = 1.6$ still exhibits a single-celled bubble. We do not pursue the question of whether a two-celled bubble structure in

the averaged three-dimensional results exists for higher S because of the possible influence of the proximity of the inflow boundary.

Despite the differences described above, the critical parameter combination for which breakdown is first observed is identical for axisymmetric and three-dimensional simulations, since the initial stages of breakdown are axisymmetric and the helical-like perturbations require some time to acquire significance. However the same differences might be responsible for hysteretic effects, for example when decreasing the swirl parameter of a three-dimensional breakdown mode.

3.2.2. *Winding sense of helical modes*

All physical and numerical experiments agree that, relative to the observer, the coherent breakdown structure (e.g. figure 12) rotates in a periodic fashion about its axis in the same direction as the ambient flow. In contrast, as will be discussed in detail below, the winding sense of the single helical or of the double-helical structure has been found to be different depending on the experimental setup. In this context we follow the common definition that a positive azimuthal wavenumber $m > 0$ corresponds to a case where the sense of the spiral follows the swirling flow in which it is embedded. In contrast, $m < 0$ modes represent cases in which the sense of the spiral is opposite to that of the swirling surrounding flow.

Classical experimental investigations in diverging tubes with a guide-vane apparatus imparting the swirl to the flow have been reported by Sarpkaya (1971*a*, *b*). He finds a $m > 0$ sense of the single helix, which is confirmed by Faler & Leibovich (1977) using a similar tube-and-vane apparatus. Moreover, the latter authors find a $m > 0$ sense for the double-helical breakdown mode.

In contrast to the above results, Lambourne & Bryer (1961) consider unconfined vortices emanating from the leading edge of a delta wing. For this experimental setup they discover a $m < 0$ orientation of the breakdown helix. This result is confirmed by Escudier & Zehnder (1982) when considering vortices in a vortex tube with tangential entry. Interestingly they also observe 'prebreakdown' disturbances exhibiting a single as well as a double helical structure with opposite, i.e. $m > 0$ orientation. Finally, the experimental results of Brücker (1993) obtained in a tube-and-vane apparatus similar to the classic one employed by Sarpkaya and Faler & Leibovich exhibit a winding sense of $m < 0$ in contrast to the aforementioned investigators. This might be related to the application of a cylindrical tube with a convergent–divergent insert in Brücker's case as opposed to the divergent tube used by Sarpkaya and Faler & Leibovich. Thus it is clear that slightly different flow fields can render diametrically opposed orientations of the breakdown helices.

Helical as well as double-helical breakdown modes presented in figure 9 exhibit a negative winding sense of $m = -1$ and $m = -2$, respectively. The single helical mode $m = -1$ exhibited by the reference case ($S = 1.095$) is most easily seen in the perspective view of the vorticity lines (figure 6), while $m = -2$ for the example $S = 1.3$ is best seen in figure 12. Hence we confirm the observations of Escudier & Zehnder (1982) and Gursul (1996) that breakdown helices originating at a locally wake-like profile have negative winding sense, while 'prebreakdown' helices located at jet-like profiles might exhibit a positive winding sense.

3.3. *Influence of coflow parameter* α

Figure 16 shows streakline visualizations obtained for the parameters $Re = 200$, $S = 1.095$, and $\alpha = 0.8$, 1.2, 1.3 and 1.6 from top to bottom, respectively. All frames displayed are taken at the time $t = 1205$. The case with the wake-like axial velocity

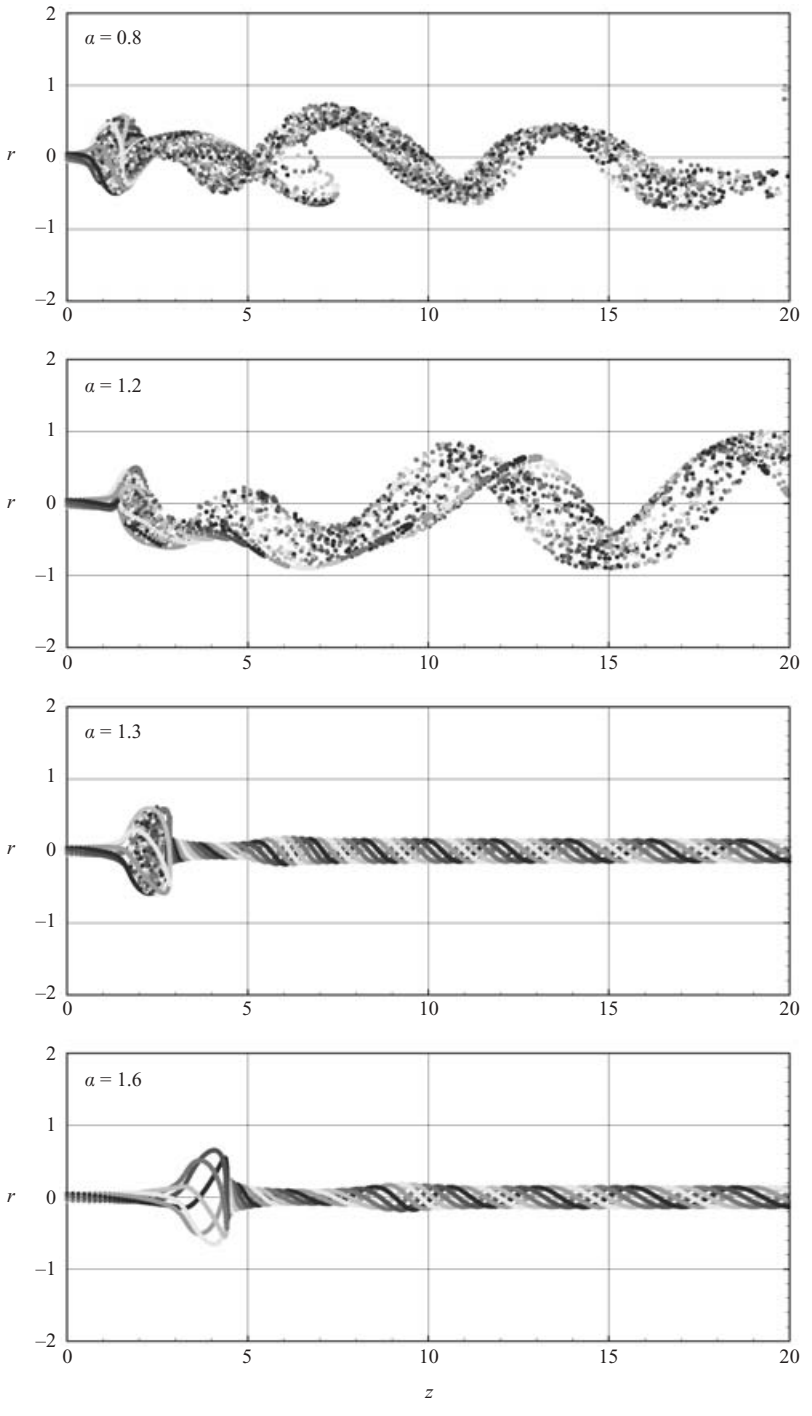

FIGURE 16. $Re = 200$, $S = 1.095$, and $\alpha = 0.8$, 1.2, 1.3, 1.6: a snapshot of the streaklines at time $t = 1205$. The case with the wake-like axial velocity profile ($\alpha = 0.8$) exhibits an unsteady helical breakdown mode switching between $m = -1$ and $m = -2$. The jet-like profiles exhibit a single helix ($m = -1$) until the value $\alpha = 1.2$. More pronounced axial velocity excess on the axis ($\alpha = 1.3$ and $\alpha = 1.6$) stabilizes the axisymmetric bubble breakdown mode and no transition to a helical mode is found to take place.

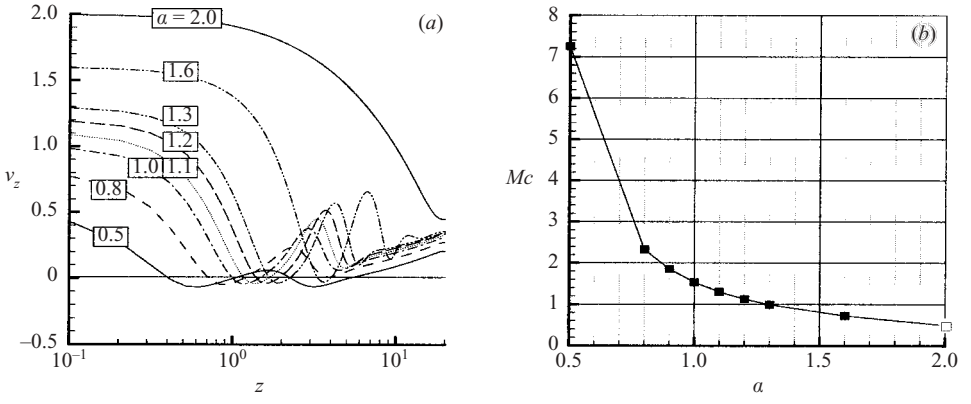

FIGURE 17. $Re = 200$, $S = 1.095$ and different coflow parameter α. All cases consider steady-state, axisymmetric results. (*a*) Axial velocity component v_z on the axis as function of z. Typically two stagnation points, i.e. a single breakdown bubble, are observed. Note however that the strongest wake case ($\alpha = 0.5$) exhibits four stagnation points corresponding to two breakdown bubbles, while the strongest jet case ($\alpha = 2.0$) does not exhibit any stagnation point at all. Further, the most upstream stagnation points move monotonically to larger z for larger values of α. (*b*) Momentum-balance model of Mahesh (1996) for the same cases discussed in (*b*) where the filled and open symbols correspond to the breakdown and no breakdown scenario, respectively. Applied at an axial position close to the inflow boundary ($z = 0.1$), the inviscid criterion mirrors the general trend between axial velocity character and onset of breakdown, although the exact threshold value is modified due to viscous effects.

profile ($\alpha = 0.8$) exhibits an unsteady helical breakdown mode emerging from an axisymmetric bubble breakdown at earlier times. A single helix ($m = -1$) exists while a new helix is born with 180° phase shift (displayed case). For a short time a double-helical $m = -2$ breakdown mode exists; however the older helix ceases quickly, leaving the newer one alone to form a single helical breakdown. This configuration gives birth to a new helix with 180° phase shift, restarting the cycle.

The second case displayed in figure 16 employs a jet-like axial velocity profile with coflow parameter $\alpha = 1.2$. Here, the axisymmetric bubble breakdown state becomes unstable, forming a single helix winding in the opposite direction to the surrounding fluid velocity, i.e. $m = -1$. The winding sense remains the same for both wake- and jet-like inflow profiles, since the helices always emerge first in the wake of the bubble, suggesting a negative winding sense (Gursul 1996). Increasing the axial velocity excess inside the core radius to $\alpha = 1.3$ stabilizes the axisymmetric breakdown, and no helical mode emerges until the simulation is stopped at $t = 2000$. Further increase of the coflow parameter to $\alpha = 1.6$ renders a bubble larger in diameter which is located considerably more downstream than the cases discussed above.

The shift of the axisymmetric bubble to locations further downstream as α increases is confirmed by the axisymmetric steady-state results considered in figure 17(*a*). Note that in contrast to the observation for varying S, the axisymmetric steady-state breakdown bubbles always have a one-celled morphology. Here, the most upstream stagnation points move monotonically to larger z for larger α. Note in particular that the strongest wake case ($\alpha = 0.5$) shown exhibits four stagnation points corresponding to two breakdown bubbles, while the strongest jet case ($\alpha = 2.0$) does not exhibit any stagnation point at all. Thus for $\alpha = 2$, no breakdown is observed in the axial extent $Z_d = 20$ considered.

This is in qualitative agreement with the momentum-balance model of Mahesh (1996) in which he suggests that breakdown occurs if the axial pressure rise exceeds the upstream momentum flux, thereby stagnating the flow. Assuming an inviscid axisymmetric flow, the one-dimensional momentum equation approximates the flow around the centreline, such that $p + \rho v_z^2$ has to remain constant along the axis. Then a criterion for the *existence of vortex breakdown* can be formulated (Mahesh 1996) which in dimensionless quantities takes the form

$$Mc = \frac{p_\infty - p_c(z)}{v_{z,c}^2(z)} \geqslant 1. \tag{3.1}$$

Here p_∞ and p_c are the pressure at infinity and at $r = 0$, respectively, while $v_{z,c}$ represents the axial velocity at $r = 0$. Therefore, an excess of axial momentum (jet-like) in the jet core delays breakdown, while a momentum deficit (wake-like) makes the vortex more susceptible to breakdown.

Figure 17(*b*) illustrates Mahesh's criterion for the axisymmetric steady-state results presented in (*a*) taken at the axial position $z = 0.1$. Simulations employing wake-like inflow profiles, as well as jet-like inflow profiles up to about $\alpha = 1.3$, clearly exhibit insufficient axial momentum to overcome the axial pressure rise, i.e. they exhibit breakdown. The case $\alpha = 1.6$ is particularly interesting, since the inflow profile supplies enough axial momentum, according to Mahesh's criterion, but stagnates nevertheless. Since no external pressure gradient is applied in the current investigation (figure 7*a*) viscosity, diffusing momentum away from the axis, is the mechanism leading to profiles exhibiting a lack of axial momentum which ultimately leads to breakdown. This viscous mechanism is evidently unaccounted for in Mahesh's inviscid criterion. Finally, the strongest jet-like inflow profile ($\alpha = 2.0$) considered does not stagnate within the present computational domain length.

3.4. *Influence of Reynolds number Re*

The present axisymmetric simulation of an unconfined swirling flow exhibits a characteristic bifurcation sequence as the Reynolds number Re grows. As a typical example the parameters $S = 1.095$ and $\alpha = 1.0$ are kept constant while Re is varied from $Re = 1$ to 500, cf. figure 18. No breakdown bubble emerges for the two lowest Reynolds numbers $Re = 1$ and 10. As Re is increased further to $Re = 100$, a single breakdown bubble is observable which increases in size as the Reynolds number takes the value $Re = 200$. In addition, a secondary swelling in the wake of the primary bubble becomes more prominent, which finally gives rise to a second bubble for even higher Reynolds numbers ($Re = 300$ and 500).

While the above Reynolds numbers yield a steady flow field, increasing Re to $Re = 1000$ renders the axisymmetric flow temporally periodic. During a period the axisymmetric breakdown bubbles shrink and expand periodically with a characteristic phase shift between each bubble, see Chen (2000) for further details.

The steady axisymmetric flow fields discussed in figure 18 compare favourably with those of experiments conducted in closed cylindrical containers with one rotating endwall. The flow produced in such closed devices is determined by the aspect ratio H_{cy}/R_{cy} and rotational Reynolds number $Re_{cy} = \Omega_{cy} R_{cy}^2/\nu$, with H_{cy} being the cylinder length, R_{cy} its radius, Ω_{cy} the angular velocity of the endwall and ν the kinematic viscosity of the contained fluid. For a sufficiently large aspect ratio H_{cy}/R_{cy} Escudier (1984) found experimentally a typical bifurcation sequence in the topology as Re_{cy} is increased. For the lowest Re_{cy} considered they observe a central viscous vortex core without any sign of breakdown. Increasing Re_{cy} leads to a well-defined vortex

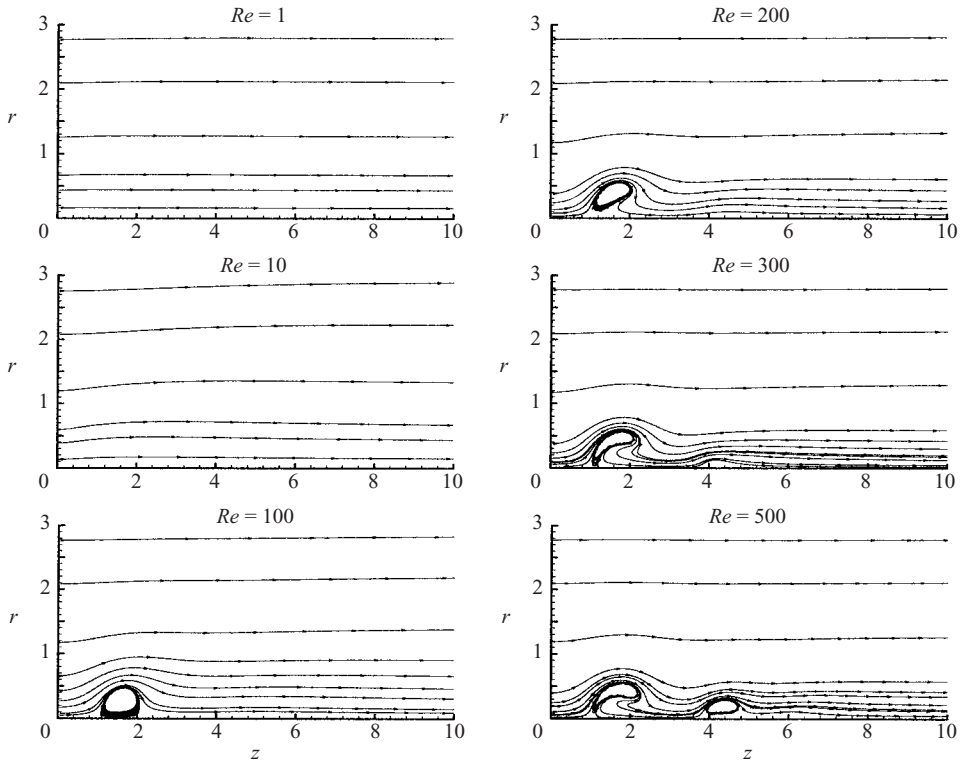

FIGURE 18. $S = 1.095$, $\alpha = 1.0$ and $Re = 1$, 10, 100, 200, 300, and 500. Similar to the observations in a closed cylindrical container with one rotating endwall, a well-ordered sequence of bifurcations exhibiting an increasing number of steady breakdown bubbles is obtained for the present axisymmetric simulation of an unconfined swirling flow.

breakdown bubble exhibiting two stagnation points: one upstream of a zone of near-stagnant recirculating fluid and the other terminating this zone downstream. Further increase of Re_{cy} gives rise to two, occasionally three, breakdown bubbles. For these values of Re_{cy} the flow is steady, while a further increase leads to a time-dependent axisymmetric periodic oscillation and finally, for yet higher rotation, to turbulence.

We wish to point out that in contrast to Re_{cy} the Reynolds number Re in the present case is formed with the axial velocity. Therefore, a similar bifurcation sequence leading to multiple breakdown bubbles is obtained for the swirl parameter S, cf. figures 3 (single bubble) and 13 (two bubbles) for $S = 1.095$, 1.3 and 1.6, respectively.

These experimental results have been confirmed numerically by Lopez (1990) and Lopez & Perry (1992) for axisymmetric simulations, and later by Marques & Lopez (2001) and Serre & Bontoux (2002) for three-dimensional simulations. The three-dimensional simulations confirm a slight precession of the multiple breakdown bubbles observed by Escudier (1984) for large enough aspect ratio and sufficiently high Reynolds number Re_{cy}.

In the present three-dimensional simulations the bubble located further downstream quickly becomes unstable to helical disturbances, ultimately leading to helical breakdown modes as will be discussed below. Therefore, in open flows we expect multiple breakdowns only as a transient feature when increasing Re or S. This has

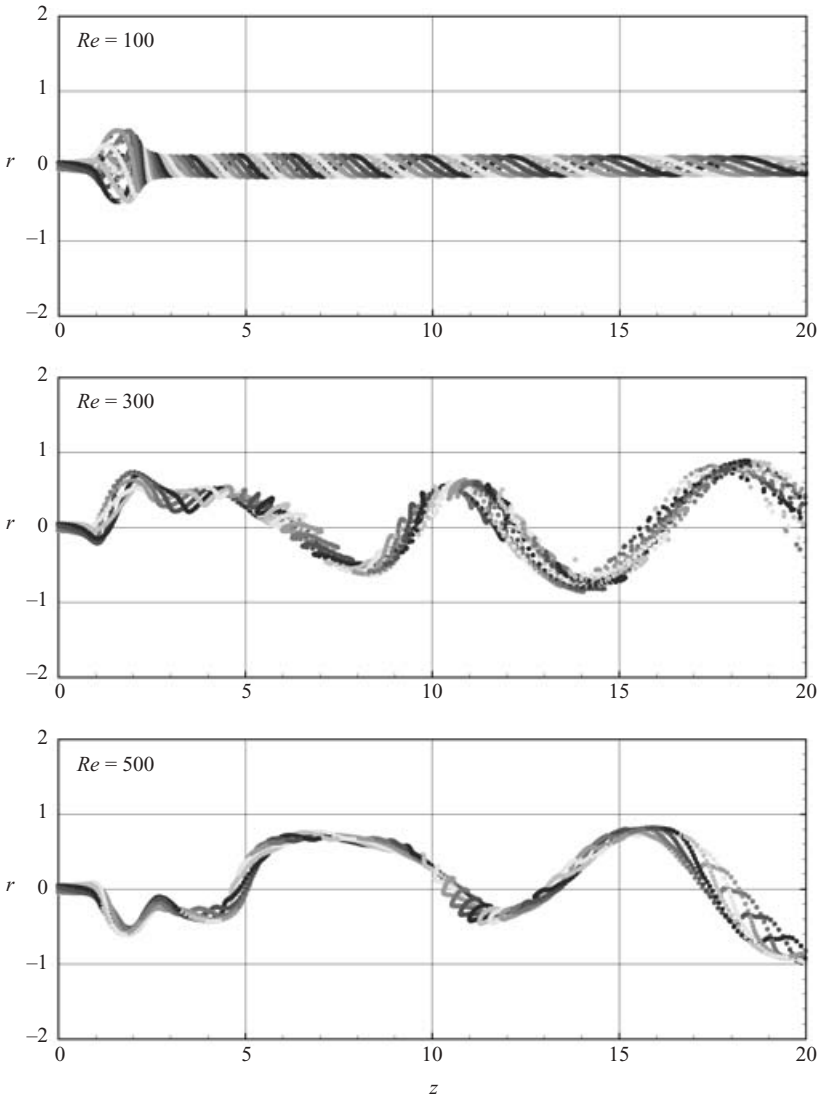

FIGURE 19. $S = 1.095$, $\alpha = 1$, and $Re = 100$, 300, and 500: a snapshot of the streaklines at time $t = 600$. The lowest Reynolds number case ($Re = 100$) remains axisymmetric and forms a steady bubble breakdown. Increasing the Reynolds number to $Re = 300$ and $Re = 500$ renders the quasi-steady axisymmetric bubble breakdown helically unstable which ultimately leads to a helical breakdown mode with $m = -1$.

been experimentally confirmed by Sarpkaya (1971*b*) using a guide-vane and tube apparatus.

Figure 19 presents three-dimensional results for some of the axisymmetric simulations discussed above ($S = 1.095$, $\alpha = 1$, and $Re = 100$, 300 and 500) by means of a streakline visualization. For the lowest Reynolds number employed, $Re = 100$, a stable axisymmetric bubble breakdown is obtained. Increasing the Reynolds number to $Re = 200$ (reference case), $Re = 300$, and $Re = 500$ ultimately yields a single helical $m = -1$ breakdown mode after the quasi-steady axisymmetric bubble breakdown configuration becomes helically unstable. In all cases this instability becomes first

visible in the wake of the most upstream bubble, similar to the reference case discussed in figure 4. For $Re = 300$ and $Re = 500$, the $m = -1$ perturbation wave propagates into the most upstream bubble, rendering a helical breakdown which exhibits an 'abrupt kink', cf. Faler & Leibovich (1977). Thus, in contrast to the reference case $Re = 200$, no remainder of the initial bubble breakdown is left visible.

We wish to point out that, while the simulations with Re below the reference case ($Re = 200$) and $Re = 300$ employed the same computational grid and time step discussed in § 2, the case $Re = 500$ is resolved by $n_r = 97$, $n_\theta = 97$, $n_z = 385$ grid points in the radial, azimuthal and axial directions, which requires a smaller time step $\Delta t = 0.01$. In contrast, the size of the domain (radius $R_d = 10$ and length $Z_d = 20$) is kept constant.

Figure 20 shows streakline visualizations of three-dimensional simulations employing a higher swirl parameter $S = 1.3$ with unchanged $\alpha = 1$ at $Re = 100$, 120, 150 and 300. As before, the lowest Reynolds number $Re = 100$ renders a stable axisymmetric bubble breakdown. Increasing the Reynolds number to $Re = 120$ yields a single helical $m = -1$ breakdown mode after the quasi-steady axisymmetric bubble breakdown configuration becomes helically unstable. Another, slightly higher Reynolds number, $Re = 150$, finally leads to a double helical $m = -2$ breakdown mode, similar to that discussed in § 3.2 for $Re = 200$. The double-helical breakdown mode $m = -2$ remains predominant even if the Reynolds number is increased further to $Re = 300$, cf. figure 20 (last frame).

4. Onset of vortex breakdown

This section complements the mechanistic explanations of vortex breakdown by Brown & Lopez (1990) and Mahesh (1996), §§ 3.1.1 and 3.3, respectively, by also discussing more theoretical concepts. Several theories have been proposed to explain the existence of vortex breakdown; however, to date none has been generally accepted. One school of thought relates breakdown to hydrodynamic instability of the vortical flow. Escudier (1988) points out that experimental evidence suggests that flow upstream of the breakdown is at worst marginally stable. Therefore it does not lend much support to the view that vortex breakdown is in any sense a direct consequence of instability. Further, breakdown has the appearance of a sudden transition, much like a shock wave or hydraulic jump. There is no evidence of the slow continuous growth typical of hydrodynamic instability. Note that this is different from the mechanism of breakdown mode selection, as will be discussed in § 5.

The abruptness of vortex breakdown suggests the existence of a *critical state* which separates a supercritical from a subcritical flow state. Here, supercritical vortex cores exclusively support downstream travelling waves while standing axisymmetric waves exist only on subcritical velocity profiles, cf. Benjamin (1962). Experimental investigations (e.g. Sarpkaya 1971*a*; Escudier *et al.* 1982; etc.) confirm that breakdown represents a transition from supercritical to subcritical flow. Starting from the axisymmetric steady Euler equations the dimensionless Squire–Long (Bragg–Hawthorne) equation is derived as

$$\frac{\partial^2\psi}{\partial z^2} + \frac{\partial^2\psi}{\partial r^2} - \frac{1}{r}\frac{\partial\psi}{\partial r} = r^2\frac{\mathrm{d}H}{\mathrm{d}\psi} - K\frac{\mathrm{d}K}{\mathrm{d}\psi}, \tag{4.1}$$

with the streamfunction ψ defined as

$$v_r = -\frac{1}{r}\frac{\partial\psi}{\partial z}, \qquad v_z = \frac{1}{r}\frac{\partial\psi}{\partial r}.$$

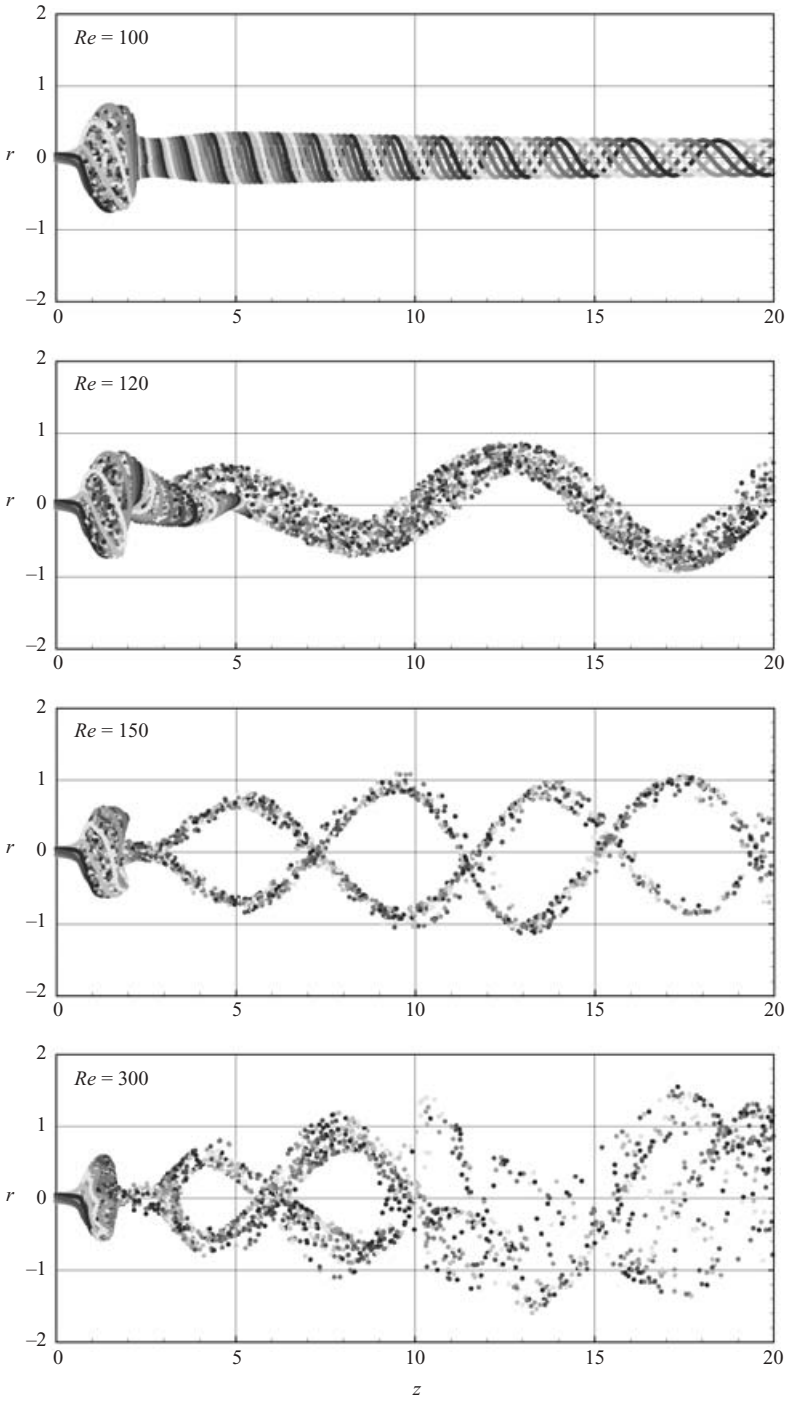

FIGURE 20. $S = 1.3$, $\alpha = 1$, and $Re = 100$, 120, 150, and 300: a snapshot of the streaklines at time $t = 900$. The lowest Reynolds number case ($Re = 100$) remains axisymmetric and forms a steady bubble breakdown. Increasing the Reynolds number to $Re = 120$ renders the quasi-steady axisymmetric bubble breakdown helically unstable, which ultimately leads to a helical breakdown mode. $Re = 150$ and $Re = 300$ undergo a similar temporal evolution as $Re = 120$, but finally settle into a double-helical breakdown mode.

The dimensionless total head is $H = p + \frac{1}{2}(v_r^2 + v_\theta^2 + v_z^2)$ while the modified circulation becomes $K = r v_\theta$.

Assuming a columnar ($\partial/\partial z = 0$, $v_r = 0$) base flow $\Psi(r)$, a stationary (i.e. time-independent) axisymmetric perturbation can be written as

$$\psi(r, z) = \Psi(r) + \epsilon\phi(r)\,\mathrm{e}^{kz}, \tag{4.2}$$

where $\epsilon \ll 1$ is the perturbation parameter, k is the complex axial growth rate ($k = k_r + \mathrm{i}k_i$), and ϕ is the eigenfunction. This perturbation ansatz (4.2) together with the Squire–Long equation (4.1) yields

$$\frac{\mathrm{d}^2\phi}{\mathrm{d}r^2} - \frac{1}{r}\frac{\mathrm{d}\phi}{\mathrm{d}r} + \left[k^2 + \frac{1}{r^3\bar{v}_z^2}\frac{\mathrm{d}(r\bar{v}_\theta)^2}{\mathrm{d}r} - \frac{r}{\bar{v}_z}\frac{\mathrm{d}}{\mathrm{d}r}\left(\frac{1}{r}\frac{\mathrm{d}\bar{v}_z}{\mathrm{d}r}\right)\right]\phi = 0, \tag{4.3}$$

keeping terms of order ϵ, i.e. linearizing in ϵ. Here the overbars represent base-flow velocity components. Benjamin (1962), invoking general properties of the Sturm–Liouville system constituted by equation (4.3), shows that the perturbation can always take an infinite number of forms with real exponential dependence on z (i.e. with $k^2 > 0$), but there is a limited possibility of standing (neutral) waves (i.e. with $k^2 < 0$ so that k is purely imaginary $k = \mathrm{i}k_i$). Thus the long-wave limit $k = 0$ separates supercritical flows ($k^2 > 0$) that cannot support standing waves and subcritical flows ($k^2 < 0$) that can support standing waves. Considering k^2 as a free parameter, he derives the criticality condition

$$\frac{\mathrm{d}^2\phi_c}{\mathrm{d}r^2} - \frac{1}{r}\frac{\mathrm{d}\phi_c}{\mathrm{d}r} + \left[\frac{1}{r^3\bar{v}_z^2}\frac{\mathrm{d}(r\bar{v}_\theta)^2}{\mathrm{d}r} - \frac{r}{\bar{v}_z}\frac{\mathrm{d}}{\mathrm{d}r}\left(\frac{1}{r}\frac{\mathrm{d}\bar{v}_z}{\mathrm{d}r}\right)\right]\phi_c = 0, \tag{4.4}$$

and points out that the homogeneous linear equation (4.4) delivers the 'test function' ϕ_c completely except for an arbitrary constant multiplier. Thus, following Reyna & Menne (1988), we choose the boundary conditions to be $\phi_c(r = 0) = 0$ and $\mathrm{d}\phi_c(r = 0)/\mathrm{d}r = 1$, where the latter is arbitrarily chosen to exclude the trivial solution. Considering Sturm's fundamental comparison theorem, Benjamin shows for pipe flows that a necessary and sufficient condition for the existence of standing waves of finite length (i.e. for a subcritical state) is that ϕ_c has to vanish at least once in the interval $0 < r < R_{bd}$, where R_{bd} is the pipe radius. Mager (1972) applies Benjamin's analysis to radially unbounded flows (the present case) by taking R_{bd} equal to the characteristic core radius, i.e. here $R_{bd} = 1$. It is important to realize that it is the values of ϕ_c within the core region that are important in determining the criticality of the flow since the ability of rotating flows to support waves depends on the magnitude of the vorticity, cf. Escudier *et al.* (1982). The outer regions of near-zero vorticity do not contribute substantially to the characteristics of the wave guide.

In contrast to Grabowski & Berger (1976), who determined the criticality character of the inflow profile only, we apply the criticality condition (4.4) to velocity profiles obtained at different axial positions of the axisymmetric steady-state solutions. This is demonstrated in figure 21 for $\alpha = 1.0$ and $Re = 200$. The left-hand column displays projected streamlines obtained at various swirl numbers S from the axisymmetric simulations. The right-hand column shows the corresponding criticality character of the velocity profiles as function of the axial coordinate z by means of a critical radius r_{crit}. The critical radius r_{crit} is equal to the radial position where the test function ϕ_c vanishes. Thus, with the above definition, the flow is subcritical if $r_{crit} < 1$ and supercritical if $r_{crit} > 1$.

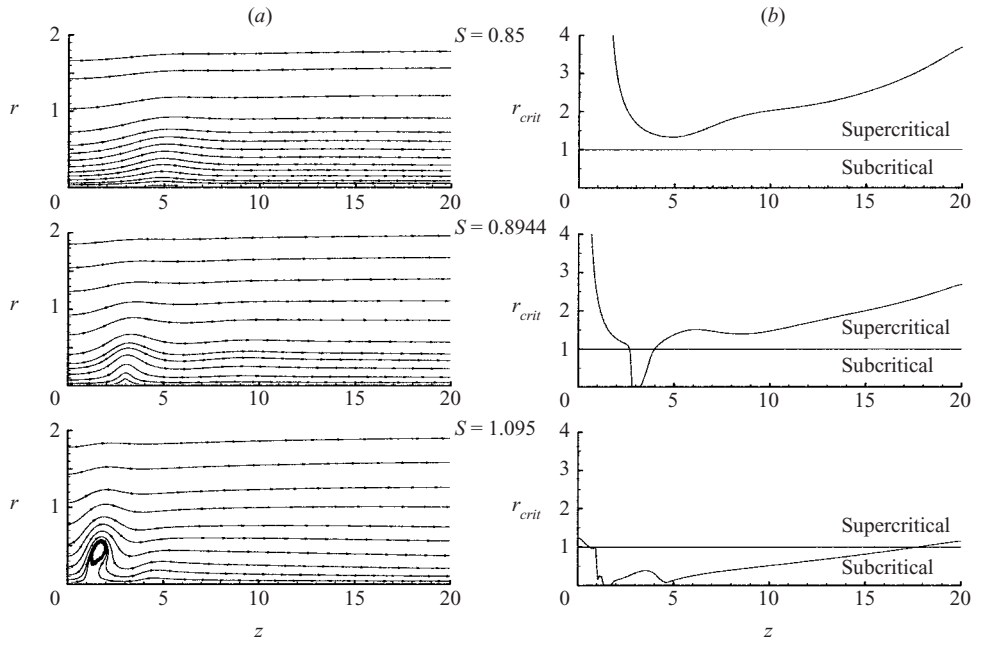

FIGURE 21. (*a*) Projected streamlines obtained from the axisymmetric simulations together with (*b*) the criticality of the vortex core for a swirl number exhibiting no breakdown ($S = 0.85$), higher swirl $S = 0.8944$ displaying an internal stagnation point and the reference case $S = 1.095$ with large recirculation zone. Assuming a supercritical inflow profile, vortex breakdown is located at the transition to a subcritical vortex core.

The lowest swirl considered ($S = 0.85$) exhibits no internal stagnation point, and the velocity profile remains supercritical everywhere. On increasing the swirl parameter to $S = 0.8944$, an internal stagnation point is observed. This is in agreement with the results of Grabowski & Berger. The flow becomes subcritical upstream of the stagnation point and recovers its supercritical character downstream. Although the columnar assumption is clearly violated around the stagnation point, breakdown is connected to a supercritical/subcritical transition as advocated by Benjamin. As the swirl is increased further ($S = 1.095$), breakdown becomes more pronounced and a large recirculation bubble exists. Obviously the flow is not columnar over a large axial extent. In particular the extent of the columnar approach flow, as required in Benjamin's analysis, becomes shorter as the swirl is increased, causing the breakdown to occur further upstream. Nevertheless a transition from super- to subcritical is still observed and the axial extent over which standing waves are supported is significantly larger than for the lower swirl considered before.

Increasing the swirl to $S = 1.3$ finally renders the inflow profile subcritical, cf. figure 22, in accordance with the results of Mager and Grabowski & Berger. A pronounced bubble can be seen, despite the lack of a supercritical/subcritical transition. However the existence of very large axial gradients and the non-existence of a columnar approach flow renders Benjamin's analysis invalid. In this regard, as mentioned above, we wish to stress that the results obtained with subcritical inflow boundary conditions should be considered with some caution, since their steady character might affect the breakdown where it is close.

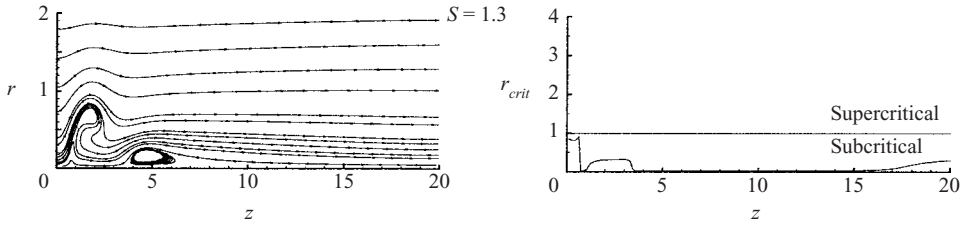

FIGURE 22. Criticality characteristic displayed in the same fashion as in figure 21 for even higher swirl $S = 1.3$. The high swirl parameter yields a breakdown which is located close to the inflow boundary. No supercritical/subcritical transition in Benjamin's framework heralds the vortex breakdown because of the lack of a columnar approach flow.

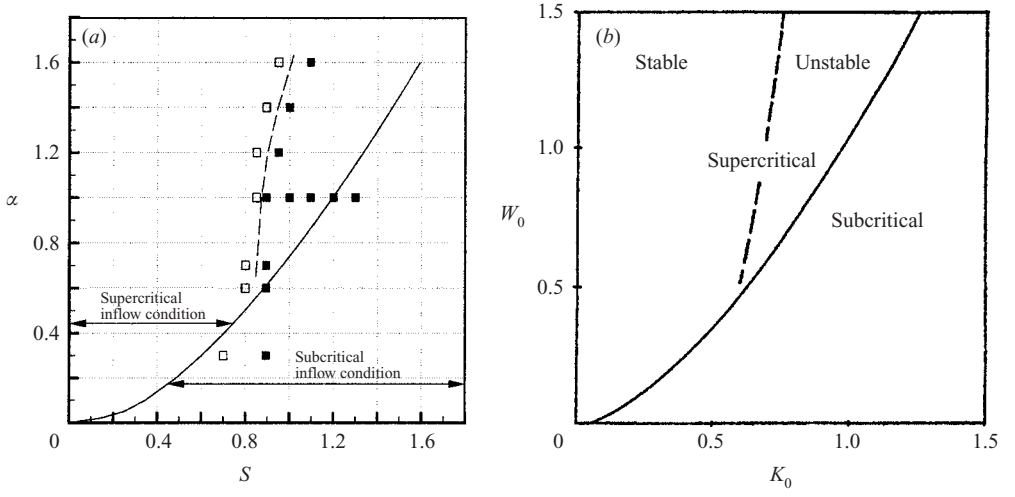

FIGURE 23. Criticality character of the vortex as defined by Benjamin (1962). (*a*) Reproduction of the criticality of the inflow profile (solid line) superposed with values of α and S obtained from axisymmetric steady-state simulations at $Re = 200$ for which (solid symbols) and for which no (open symbols) internal stagnation point has been observed. No correlation between the occurrence of breakdown and the super- and subcritical character of the inflow profile is found; however applying the criticality condition locally yields excellent agreement for supercritical inflow (dashed line). (*b*) Difference between inviscid criticality condition (solid line) and failure of viscous QCA (dashed line) in a K_0, W_0 (S, α) parameter space (reprinted from Shi & Shan 1987 with the permission of ALSTOM (Switzerland) Ltd., the successor of BBC). The difference due to viscosity is qualitatively similar to the difference observed between inflow and local criticality character (*a*) which strengthens the suggestion of Grabowski & Berger that viscosity drives the flow toward criticality and subsequently causes it to break down.

Figure 23 reproduces the criticality of the inflow profile (solid line) presented before by Mager (1972) and Grabowski & Berger (1976). Superposed on that figure are the values of α and S obtained from axisymmetric steady-state simulations at $Re = 200$ for which (solid symbols) and for which no (open symbols) internal stagnation point, i.e. vortex breakdown, has been observed. The obtained results agree very well with those of Grabowski & Berger who find no correlation between the occurrence of breakdown and the super- and subcritical character of the inflow profile.

In contrast the dashed line in figure 23 marking the boundary between breakdown and non-breakdown parameter combinations is obtained by applying the criticality

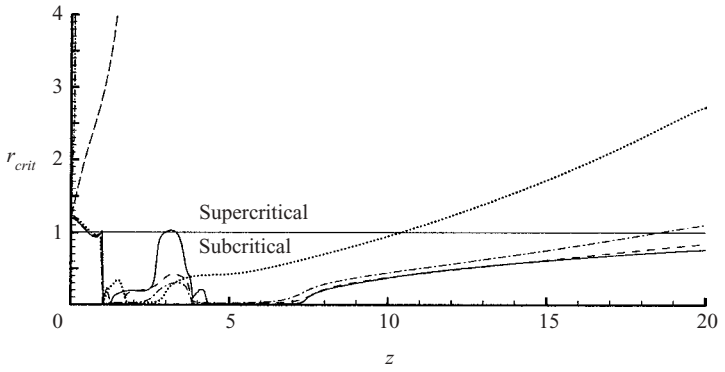

FIGURE 24. Criticality characteristic of the axisymmetric vortex core in terms of r_{crit} for $S = 1.095$, $\alpha = 1.0$, and several Reynolds numbers Re. Solid line: $Re = 500$, dashed line: $Re = 300$, dash-dotted line: $Re = 200$, dotted line: $Re = 100$, long-dashed line $Re = 10$, dash-dot-dotted line: $Re = 1$. Application of the inviscid Benjamin criterion to the local, viscously diffused velocity profile effectively renders it viscous. Depending on Re the flow undergoes the same number of supercritical/subcritical transitions as the number of breakdown bubbles observed.

condition (4.4) locally in the above-discussed fashion. Then, for supercritical inflow conditions, breakdown is observed exactly when a transition to subcriticality is observed locally in the axial evolution of the vortex. As mentioned before, Benjamin's analysis breaks down for subcritical inflow properties, since the breakdown is located directly at the inflow boundary and thus lacks a columnar approach flow. Apparently, Benjamin's analysis predicts the flow character far beyond its formal validity.

Another school of thought relates breakdown to flow stagnation, i.e. the failure of the quasi-cylindrical approximation (QCA), analogous to boundary layer separation (Hall 1972). Under the QCA, the radial velocity profile satisfies a linear ordinary differential equation of second order for a given axial and azimuthal velocity profile. Shi & Shan (1987) point out that the equation giving the radial velocity profile has merely one term more than the equation for the 'test function' ϕ_c as defined by Benjamin. This viscosity-related term causes the point of failure of the QCA to precede the critical point.

Thus the QCA can be viewed as a viscous extension of Benjamin's criticality criterion. Figure 23(*b*) reproduces a result presented by Shi & Shan (1987) where the solid line corresponds to the criticality locus of Benjamin and the dashed line represents the failure of the viscous QCA in a K_0, W_0 (S, α) parameter space. Interestingly, the difference due to viscosity is qualitatively similar to the difference observed between inflow and local criticality character (figure 23*a*). This strengthens the suggestion of Grabowski & Berger that in the absence of an externally imposed pressure gradient, viscosity drives the flow toward criticality and subsequently causes it to break down.

In § 3.4 it is demonstrated that depending on the Reynolds number employed, for the same S, α parameter pair the axisymmetric steady-state solution can exhibit no, one or two breakdown bubbles. Since Benjamin's criticality condition assumes inviscid dynamics, questions concerning the validity of the condition arise. However, as discussed above, application of the criterion to the local viscously diffused velocity profile effectively renders the inviscid criterion viscous. This is confirmed in figure 24 which considers the criticality of the axisymmetric steady-state results discussed in § 3.4. For the two lowest Reynolds numbers $Re = 1$ (dash-dot-dotted line)

and $Re = 10$ (long-dashed line) no internal stagnation point and correspondingly no supercritical/subcritical transition is found. The intermediate Reynolds numbers $Re = 100$ (dotted line), $Re = 200$ (dash-dotted line), and $Re = 300$ (dashed line) exhibit one breakdown bubble preceded by a supercritical/subcritical transition. Finally, $Re = 500$ (solid line) exhibits two breakdown bubbles each visible as a supercritical/subcritical transition. Thus, as suggested by Benjamin, multiple breakdowns can be interpreted as a stationary wavetrain.

5. Mode selection of vortex breakdown

Suggestions have been made as early as by Benjamin (1962) that, although the essential mechanism of vortex breakdown is explainable in terms of a steady axisymmetric model, considerable disturbances from this basic situation may be important in practical situations. As proposed by Escudier *et al.* (1982), the key to understanding breakdown and its different modes observed in experiments lies in the consideration of the flow field created by the vortex breakdown itself. In the current investigation this reduces to an investigation of the stability properties of the steady vortical flow fields obtained for the axisymmetric simulation.

5.1. *Local absolute/convective stability*

An extensive review of the concepts of local absolute (AI) and convective (CI) instability and their implications for global instability of a spatially developing flow has been given by Huerre & Monkewitz (1990). In short, the terms absolute and convective describe the linear behaviour of the impulse response of an unstable medium. If an impulsively generated small-amplitude transient contaminates the entire uniform ($\partial/\partial z = 0$, $v_r = 0$) flow, it is termed absolutely unstable. In this case, a mode with zero group velocity that grows in time, i.e. is self-excited, eventually dominates the linear response. If, on the other hand, the transient or wave packet is convected away from the source and leaves the flow ultimately undisturbed, one speaks of convective instability.

The concept of AI/CI may appear to be trivial: a flow that is CI in one reference frame becomes AI in another. There is no preferred laboratory frame in uniform flows that are invariant under Galilean transformations. Hence it is precisely in situations where the Galilean invariance is broken that AI/CI instability issues acquire physical significance. This happens to be the case either when the flow is continuously forced at a specific axial location, or when it is spatially developing, or else when a no-slip boundary condition is enforced at the walls. In such cases the pertinent reference frame is unambiguously defined.

Since spatially evolving flows are typically non-uniform, difficulties arise in relating the local linear instability character to the global response of the flow. It is found that local absolute instability is necessary but not sufficient for a linear global mode to become self-excited, i.e. to grow in time, cf. Chomaz, Huerre & Redekopp (1988). Rather, a self-sustained resonance may appear via a Hopf bifurcation when the system exhibits a sufficiently large pocket of local absolute instability. A second, fully nonlinear mechanism yielding a self-sustained global mode has been identified by Pier & Huerre (2001) for sech^2 wake profiles. Here, no sufficiently large pocket of local absolute instability is necessary, and a steep global mode can be triggered as soon as local absolute instability appears.

However, Monkewitz (1988) shows the existence of a finite pocket of local absolute instability in the wake of axisymmetric bluff bodies, suggesting that the experimentally

observed helical vortex shedding is driven by a linear self-excited global mode in the near wake. The present vortical flow 'can decelerate and diverge as if a solid (axisymmetric) obstacle were met' (Hall 1972; Garg & Leibovich 1979; etc.). Thus, in some sense, the axisymmetric vortex breakdown bubble acts like a solid body and it is natural to assume that the wakes in both circumstances have similar properties, at least for certain parameter regimes, leading to a helical breakdown mode.

In the following we will discuss the local AI/CI properties of our axisymmetric steady-state results by assuming that, at any axial position, they essentially can be approximated by a Batchelor vortex (Batchelor 1964). Then, similarly to the Batchelor vortex, the flow is defined by the external flow and swirl parameter, a and q, respectively. In the present non-uniform case they take the form

$$a(z) = \frac{\tilde{v}_{z,\infty}}{\tilde{v}_{z,c} - \tilde{v}_{z,\infty}}, \qquad q(z) = \left| \frac{\tilde{v}_{\theta}(R)}{\tilde{v}_{z,c} - \tilde{v}_{z,\infty}} \right|, \tag{5.1}$$

where $a(z)$ and $q(z)$ indicates that they have to be determined locally for each axial position z. To be able to compare with the viscous (Delbende *et al.* 1998) and inviscid (Olendraru *et al.* 1996, 1999) Batchelor vortex, q has to take a positive value which has to be enforced since the denominator can take negative values in the current case.

Figure 25 displays the regions of absolute (AI) and convective (CI) instability for the viscous Batchelor vortex. These regions are bounded by solid lines indicating the absolutely unstable azimuthal wavenumbers m. Superimposed, the instability character of the present investigation employing $Re = 200$, $\alpha = 1$ and different swirl parameters S are plotted for all values of z (dash-dotted line), where the arrows point in the downstream direction. For the case with the lowest swirl $S = 0.8944$ (figure 25*a*) the only nose reaching into the AI region corresponds to the axial position $z = 3.0$. Comparison with figure 9 reveals it to be inside the bubble; however no sufficiently large pocket of absolute instability is formed, keeping the axisymmetric breakdown mode stable, cf. figure 9. On increasing the swirl parameter to $S = 1.0$ (figure 25*b*) both noses reach into the AI region, the first one at $z = 1.8$ inside the bubble and the second at $z = 5.3$ in the wake of the bubble. Note that the end of the simulation domain at $z = 20$ corresponds to the end of the dash-dotted line inside the plotted regime. Therefore axial positions upstream and around the bubble appear stretched on the dash-dotted line, while regions downstream of the bubble which no longer change rapidly appear to be squeezed. Thus the AI pocket in the wake of the bubble ($z = 5.3$) is considerably larger than the one in the bubble itself ($z = 1.8$) and also much larger than the pocket for $S = 0.8944$. This suggests that the critical size to give rise to a global mode might be reached first in the wake of the bubble. This suggestion is confirmed in figure 9 which proves the existence of a helical $m = -1$ breakdown mode for this parameter combination. Similarly to the reference case, this instability starts in the wake of the bubble. Increasing the swirl parameter further to $S = 1.095$ (figure 25*c*) and $S = 1.3$ (figure 25*d*) increases the AI pocket in the wake of the bubble further, suggesting a more pronounced helical breakdown. In addition, a larger portion of the pocket lies at higher azimuthal wavenumbers, giving rise to the possibility of breakdown modes with higher helical wavenumber. Again this is confirmed in figure 9 by a double-helical $m = -2$ breakdown mode for $S = 1.3$.

Similarly, varying the coflow parameter α instead of S affects the size and spectrum of the absolutely unstable pocket significantly. Interestingly, even for the jet case $\alpha = 1.6$ the AI region is entered from the wake side $a < 0$ due to the rapid deceleration of the axial flow close to the axis, which quickly leads to a wake-like character of the

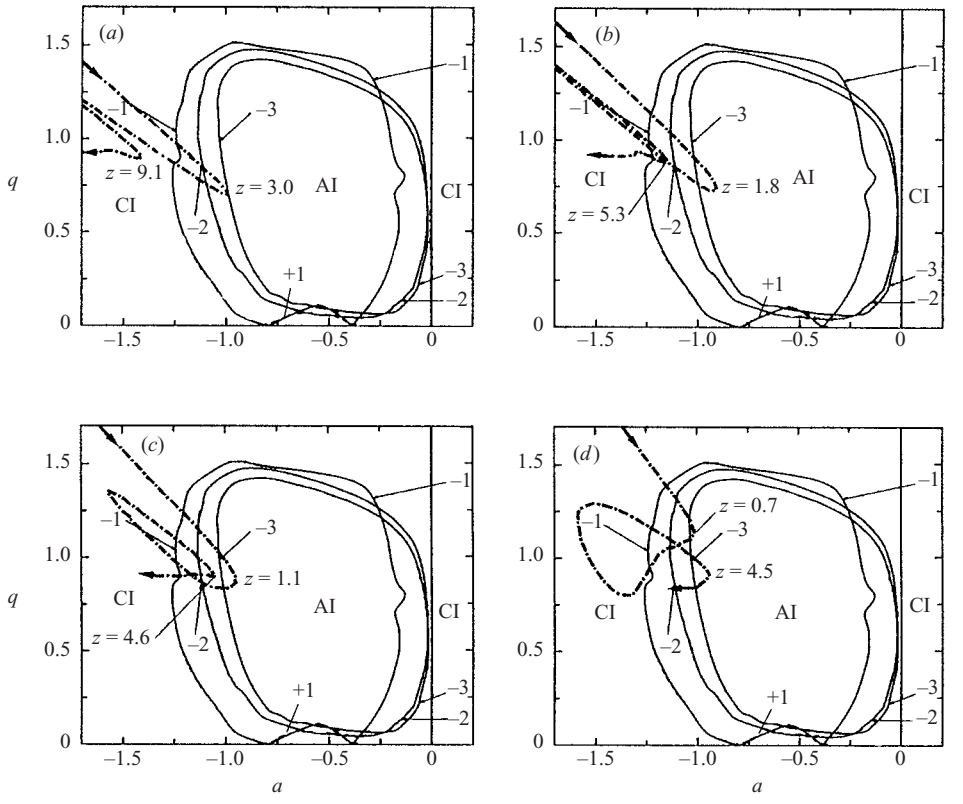

FIGURE 25. AI/CI transition curves for a Batchelor vortex in the a, q parameter space for azimuthal modes $m = \pm 1, -2, -3$. Solid lines: viscous study of Delbende *et al.* (1998). Dash-dotted line: present axisymmetric simulation with $Re = 200$, $\alpha = 1.0$ and $S = 0.8944$ (*a*), $S = 1.0$ (*b*), $S = 1.095$ (*c*), and $S = 1.3$ (*d*). Increasing the swirl parameter to higher values yields a larger pocket of absolute instability that reaches deeper into the AI region, thereby destabilizing higher azimuthal wavenumbers m. This suggests a bifurcation sequence of breakdown modes from axisymmetric to helical to double helical as observed in the current investigation. (Reprinted in modified form with the permission of the authors and Cambridge University Press.)

axial velocity profile. However, only a small pocket of absolute instability exists, which similarly to the low-swirl case is unable to support self-sustained oscillations. Therefore a stable axisymmetric breakdown is observed (figure 16). In contrast, assuming the wake-like inflow profile, $\alpha = 0.8$, yields a very large AI pocket comparable to the high-swirl cases discussed above. Similarly an unstable $m = -1$, $m = -2$ breakdown mode exists, cf. figure 16.

As noted by Delbende *et al.* (1998) the general effect of viscosity is a decrease of the area of the AI region. The low-Reynolds-number Grabowski profiles with $Re = 1$ and $Re = 10$ do not appear on the q, a parameter plot in the given extent; they are never AI. Increasing the Reynolds number to $Re = 500$, in the other extreme, yields a large AI pocket, suggesting a helical breakdown mode, which is confirmed in figure 19.

Classically, the rotational frequency of the helical breakdown mode observed in experiments is compared to temporal stability results. For example Garg & Leibovich (1979) compare their time-averaged experimental velocity profiles at several axial positions with the inviscid linear stability analysis of Lessen, Singh & Paillet (1974)

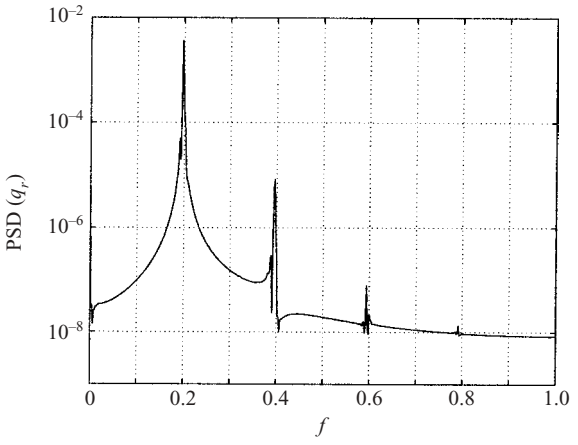

FIGURE 26. Reference case: power spectrum of the radial flux q_r at $r = 0.05$ and $z = 3.0$. Similar spectra are obtained for all three velocity components throughout the computational domain.

and find that profiles upstream of breakdown are stable to modes $m = 0$ and $m \neq 0$, while unstable to $m \neq 0$ downstream. In particular, they find that the locations of spectral peaks in the wakes agree reasonably well with the most unstable $m = -1$ mode, implying the existence of a single helix in the wake of the breakdown. However $m = -1$ is not found to be the most unstable helical mode in the inviscid temporal analyses, a feature that typically persists in the presence of viscosity. Figure 25 reveals that wake profiles downstream of the breakdown bubble are AI, an observation confirmed by Yin *et al.* (2000), among others. In particular Yin *et al.* show that the absolutely most amplified mode is $|m| = 1$ and the associated frequency agrees well with experiments.

The spectral character of the flow field for the reference case ($Re = 200$, $\alpha = 1$, $S = 1.095$) is shown in figure 26 by means of an instantaneous single-point measurement of an arbitrarily chosen velocity component, cf. Garg & Leibovich (1979). Here, as an example, the logarithm of the spectral power density (PSD) of the Fourier-transformed radial flux q_r at the location $\theta = 0$, $r = 0.05$, and $z = 3.0$ is considered. The dominant rotational frequency of the helical breakdown is obtained at $f \approx 0.2$, corresponding to a period of approximately $t = 5$ which agrees with the animation of Ruith & Meiburg (2002*a*).

The exact value of f is independent of the specific velocity component considered. Since the noise level in the numerical simulation is very low we observe spectral peaks for r significantly different from 1 and z upstream from the visible helix. However the amplitudes are orders of magnitude lower for these 'non-optimal' positions and thus are expected to be not detectable in physical experiments.

Finally, it is informative to relate the dominant frequency of the rotating helix to the azimuthal velocity component at the inflow boundary. This opens the possibility of comparing the present spectrum to the spectra of Garg & Leibovich (1979) obtained in tube-and-vane experiments. A first estimate is obtained by considering the solid body rotation Ω at the axis $r = 0$. For the Grabowski profile, an analytic expression of the form $\Omega(r = 0) = 2S$ is then obtained, which follows from the fact that $\Omega = \omega_z/2$ where ω_z is the axial vorticity. This yields a dimensionless frequency $f = 0.349$ for the reference case. Hence, this criterion overestimates the frequency, which is due to

the fact that Ω decreases rapidly within the vortex core, suggesting that an 'integral' measure over the whole core radius might be more accurate. Here, solid body rotation is assumed out to the radial position at which the azimuthal velocity component takes its maximum $r(v_{\theta,max})$. For the Grabowski profile $r(v_{\theta,max}) = \sqrt{2/3}$, thus leading to $\Omega = 4S/3$. This yields a dimensionless frequency $f = 0.232$ for the reference case, which corresponds closely to the observed rotation frequency of the helix. Further, application of the latter criterion to the experimental velocity profiles of Garg & Leibovich (1979) also yields good agreement with measured frequencies, confirming the fixed ratio between azimuthal inflow profile and observed spectral peak caused by the rotating helix.

5.2. *Global stability*

Clearly, § 5.1 can only provide a qualitative link between the instability of the axisymmetric steady vortical flow and the breakdown mode ultimately selected. Besides the apparent but solvable problem that comes with the *ad hoc* assumption that the local velocity profile matches the Batchelor vortex and the different *Re* employed, the difficulty introduced by non-uniformity ($\partial/\partial z \neq 0$, $v_r = 0$) of flow remains. It is impossible to determine how large the pocket of absolute instability has to be to sustain a self-excited global mode that eventually determines the breakdown mode selection.

Therefore, in contrast to earlier local instability investigations (Lessen *et al.* 1974; Lessen & Paillet 1974; Olendraru *et al.* 1996, 1999; Delbende *et al.* 1998; Yin *et al.* 2000; among others) we consider the entire axisymmetric vortex, exhibiting arbitrary smooth variations in the streamwise direction. Here we obtain the global linear stability characteristics directly from the (nonlinear) direct numerical simulation of breakdown, which subsequently can be compared to results obtained from a normal-mode analysis of the linearized equations, cf. Ruith & Meiburg (2002*b*) for preliminary results.

Figure 27 illustrates several different ways to obtain the time interval and magnitude of exponential growth for the example of the reference case. The simplest and most straightforward method is to take a single velocity signal at a constant location, as the three-dimensional flow evolves in time from the columnar initial condition. Taking the modulus of the difference of this signal and the axisymmetric quasi-steady (qs) state yields for the example of the azimuthal velocity component the $|\Delta v_\theta|$ signal displayed in figure 27(*a*) in the form $|\Delta v_\theta(r, \theta, z, t)| = |v_\theta(r, \theta, z, t) - v_{\theta,qs}(r, z)|$. Here, the location $\theta = 0^\circ$, $r = 0.07$ and $z = 4.95$ has been taken and the quasi-steady state is assumed to be equivalent to the axisymmetric steady state which has been converged to machine accuracy, cf. § 3.1.

The initial columnar vortex clearly evolves toward the axisymmetric state; however around $t = 500$ a helical instability takes over. Due to the azimuthal velocity component, the vortex revolves around its axis while the instability grows, causing an oscillatory growing signal for a fixed spatial location and out-of-phase sampling. However, the envelope of the signal clearly exhibits an exponential growth.

The second graph in figure 27(*a*) tracks the azimuthally averaged azimuthal velocity signal $\overline{\Delta v_\theta(r, z, t)} = (1/2\pi) \int_0^{2\pi} |\Delta v_\theta(r, \theta, z, t)| \, \mathrm{d}\theta$ at the same axial and radial position as discussed above. However, in contrast to the earlier case the initial condition is assumed to be the unperturbed axisymmetric steady state. The flow becomes unstable to helical perturbations caused by round-off errors and exhibits an exponential growth spanning twelve decades. The growth rate σ determined from the expression

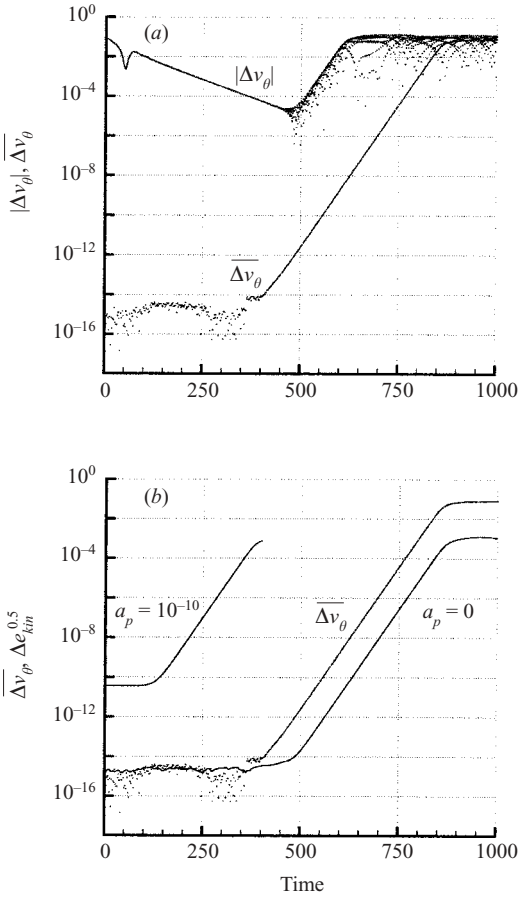

FIGURE 27. Reference case: comparison between different ways to obtain the time interval and magnitude of exponential growth. (*a*) Local azimuthal velocity probe at single azimuthal position $|\Delta v_\theta|$ as well as azimuthally averaged signal $\overline{\Delta v_\theta}$. (*b*) Comparison between local and global instability evaluation determined by the kinetic energy per mass Δe_{kin}. The growth rate σ obtained with ($a_p = 10^{-10}$) and without ($a_p = 0$) perturbation is equal to the σ evaluated locally.

$v_\theta(t+\tau) = v_\theta(\tau)\exp(\sigma t)$, where both t and τ have to be in the linear regime, agrees with the σ obtained from the envelope of the $|\Delta v_\theta|$ signal.

To stress the global character of the instability an integral measure over the entire computational domain, rather than information based on local probes, is desirable. This is realized by computing the difference of the kinetic energy per mass Δe_{kin} between the current and quasi-steady state in the form

$$(\Delta e_{kin})^{0.5} = \frac{1}{\sqrt{2}V}\int\int_V ([v_\theta(t) - v_{\theta,qs}]^2 + [v_r(t) - v_{r,qs}]^2 + [v_z(t) - v_{z,qs}]^2)^{0.5}\,\mathrm{d}V. \quad (5.2)$$

A comparison between Δe_{kin} and $\overline{\Delta v_\theta}$ is shown in figure 27(*b*). The unperturbed case $a_p = 0$, after accumulating sufficient numerical errors, grows exponentially over several decades with the same growth rate obtained for $\overline{\Delta v_\theta}$. To reduce the execution time, it is beneficial to perturb the initial axisymmetric steady-state solution with white noise in order to render the flow three-dimensional more quickly. A perturbation with

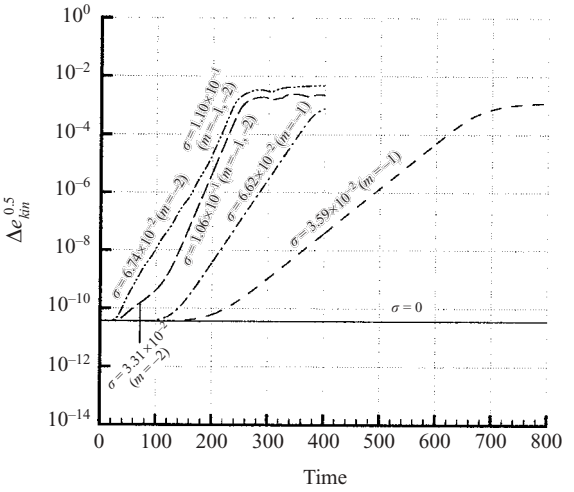

FIGURE 28. Growth rates σ for $Re = 200$, $\alpha = 1.0$, and different swirl. Solid line: $S = 0.8944$, the axisymmetric bubble breakdown base flow remains stable. Dashed line: $S = 1.0$, here the base flow becomes unstable toward the $m = -1$ mode, ultimately rendering a helical breakdown structure. Dash-dotted line: $S = 1.095$, similar to $S = 1.0$, although with larger exponential growth rate σ. Long-dashed line: $S = 1.2$, exhibits two unstable modes $m = -1$ and $m = -2$ yielding a breakdown mode which switches between double and single helical. Dash-dot-dotted line: $S = 1.3$, similar to $S = 1.2$; however streakline visualizations reveal a pulsant, double-helical breakdown structure.

amplitude $a_p = 10^{-10}$, while retaining σ, approximately halves the time for the flow to become helically unstable, thus decreasing computational cost.

The effect of the swirl parameter S on the growth rate σ and the azimuthal mode selection m starting from an initially perturbed axisymmetric base flow is illustrated in figure 28. In all simulations $Re = 200$ and $\alpha = 1.0$, and the initial perturbation amplitude $a_p = 10^{-10}$ is kept constant. For the lowest swirl parameter considered, $S = 0.8944$ (solid line), no growing helical disturbances are found and the breakdown remains axisymmetric, cf. figure 9. In contrast, the case with $S = 1.0$ (dashed line) exhibits exponential growth from approximately $t = 220$ to $t = 640$ after which Δe_{kin} saturates. The power spectral density in the azimuthal direction of an arbitrary velocity component reveals a dominant peak at $|m| = 1$.

The azimuthal wavenumber selection of $|m| = 1$ is confirmed by the eigenfunction plotted in figure 29. Here, the vorticity components obtained for the axisymmetric base flow are subtracted from the values of the three-dimensional simulation at $t = 400$ to deliver an iso-surface of the vorticity $|\omega| = 0.6$ (figure 29*a*) and the azimuthal vorticity component ω_θ in a meridional slice (figure 29*b*). We wish to point out that the time t is chosen arbitrarily and any t in the exponential growth period delivers invariant eigenfunctions. The double helix displayed in the upper frame clearly corresponds to the peaks exhibited by the modulus of a single sine or cosine function in the azimuthal direction, while a negative sign of the helix, i.e. $m = -1$, is readily seen with the definition in § 3.2.2. Further, in agreement with the local absolute/convective stability results discussed in § 5.1, the exponentially growing global mode is located in the wake of the initial bubble breakdown. Finally the ω_θ iso-contours displayed in figure 29(*b*) reveal alternating signs of the azimuthal vorticity relative to the axis. This causes an increasing asymmetry of the azimuthal vorticity distribution which leads

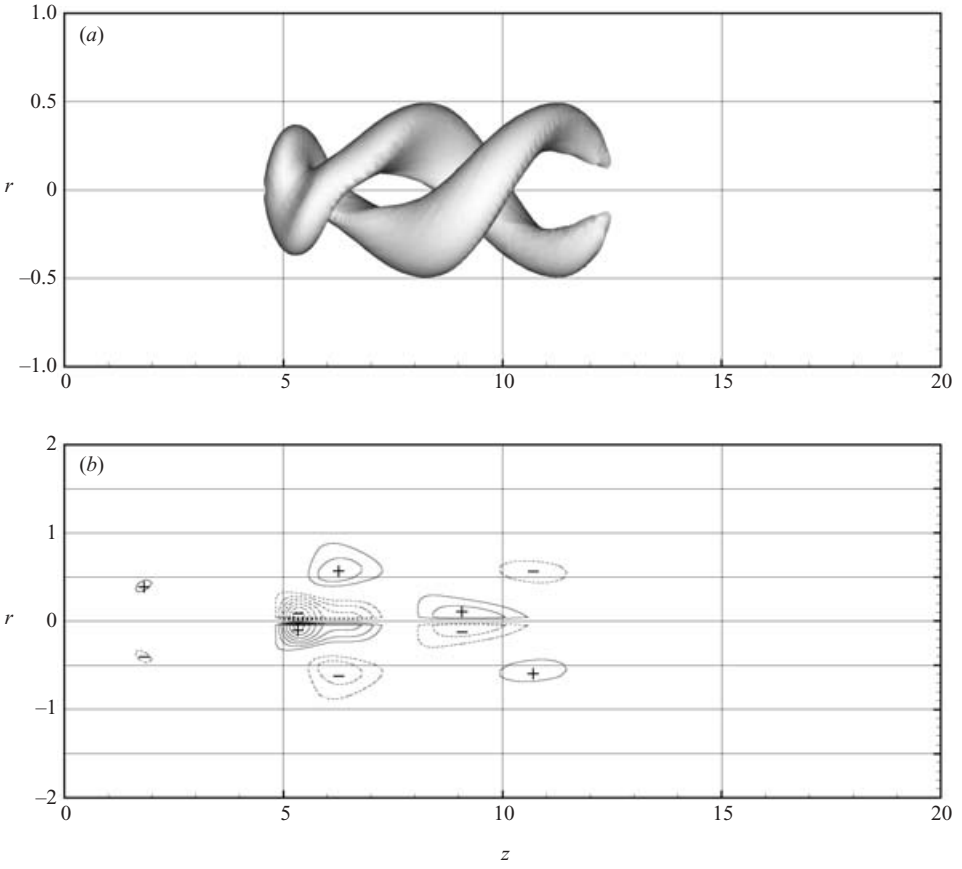

FIGURE 29. Eigenfunctions at time $t = 400$ of the case $Re = 200$, $\alpha = 1.0$, and $S = 1.0$. The iso-surface of the vorticity $|\omega| = 0.6$ (a) reveals an $m = -1$ instability mode which corresponds to alternating signs of the azimuthal vorticity (b), $\omega_\theta = \pm 0.2$–± 0.9.

ultimately to a helical breakdown mode, in analogy to the experiments of Althaus *et al.* (1995*b*).

Increasing the swirl parameter to $S = 1.095$ (reference case) does not alter the structure of the eigenfunction ($m = -1$), which is expected since both $S = 1.0$ and $S = 1.095$ render a helical breakdown mode. However the growth rate increases to $\sigma = 6.62 \times 10^{-2}$ compared to $\sigma = 3.59 \times 10^{-2}$ obtained for $S = 1.0$ (figure 28). In contrast, a yet higher swirl parameter, $S = 1.2$, exhibits two different exponential growth rates σ, suggesting the growth of two distinct instability modes. Computation of the power spectral density of a velocity signal similar to that done above reveals that the exponential growth until about $t = 100$ corresponds to an azimuthal wavenumber of $|m| = 2$.

As before, the wavenumber selection is confirmed by the eigenfunction plotted here at $t = 80$, cf. figure 30. Four equidistant helices in the azimuthal direction correspond to the peaks of a periodic function with twice the frequency as $|m| = 1$, while the sign remains unchanged, i.e. $m = -2$. Note that now the ω_θ iso-contours displayed in figure 30(b) exhibit a varicose mode starting further downstream than found for $m = -1$ above.

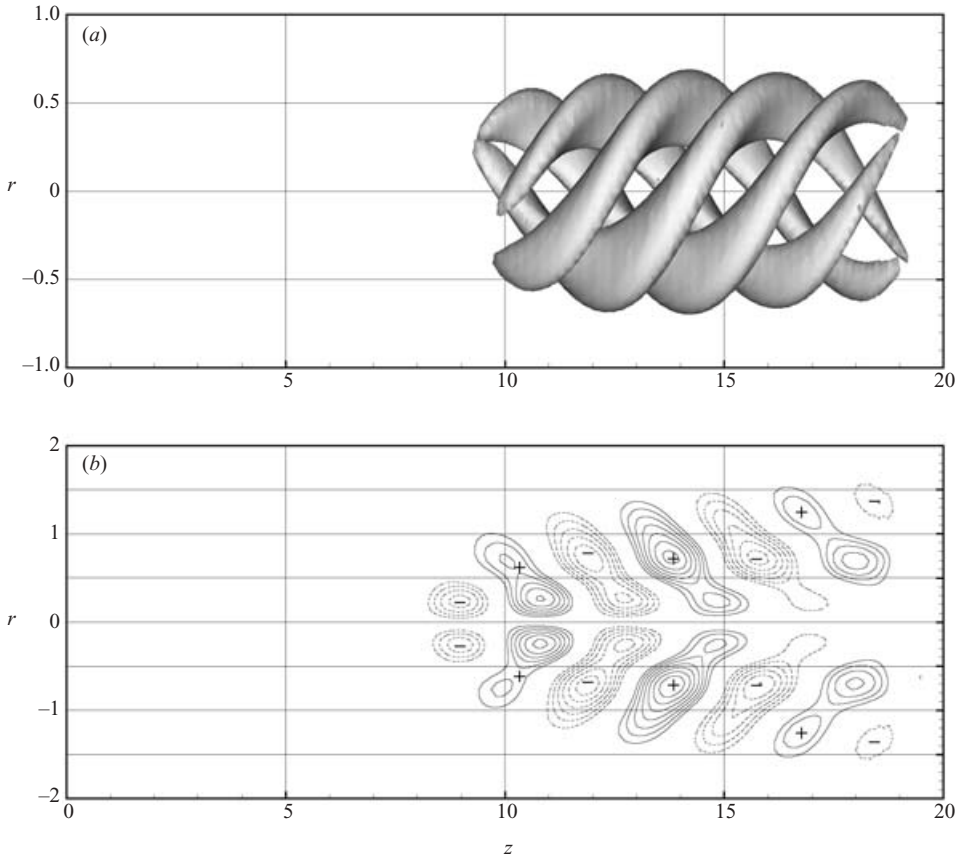

FIGURE 30. Eigenfunctions at time $t = 80$ of the case $Re = 200$, $\alpha = 1.0$, and $S = 1.2$. The iso-surface of the vorticity $|\omega| = 0.6$ (*a*) now reveals an $m = -2$ instability mode which corresponds to a varicose mode of the azimuthal vorticity (*b*), $\omega_\theta = \pm 0.3$–± 0.9.

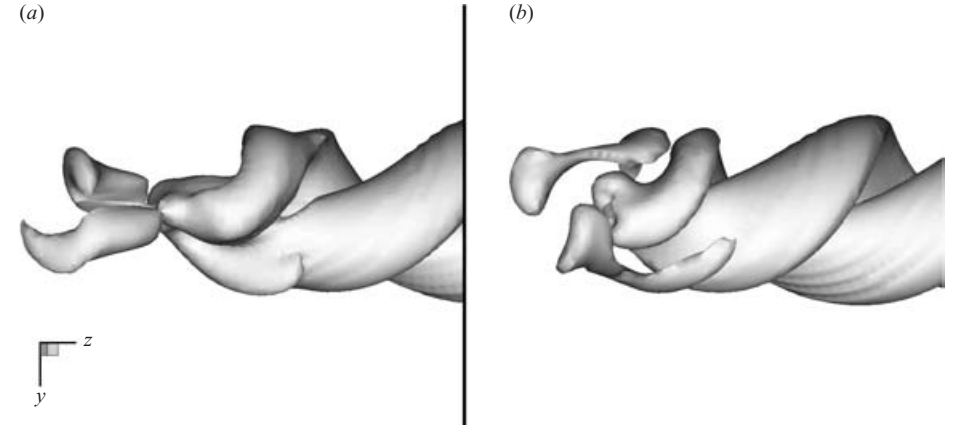

FIGURE 31. Eigenfunctions of the case $Re = 200$, $\alpha = 1.0$, $S = 1.0$ (*a*) and $S = 1.2$ (*b*) displayed at time $t = 400$ and $t = 130$, respectively. Here a visualization by means of λ_2 iso-surfaces is beneficial since $|\omega|$ of the $m = -1$ and $m = -2$ mode at $S = 1.2$ differ significantly and a selection of a value for $|\omega|$ to display both at the same time is impossible. In contrast, the lower swirl case $S = 1.0$ only exhibits an eigenfunction corresponding to $m = -1$.

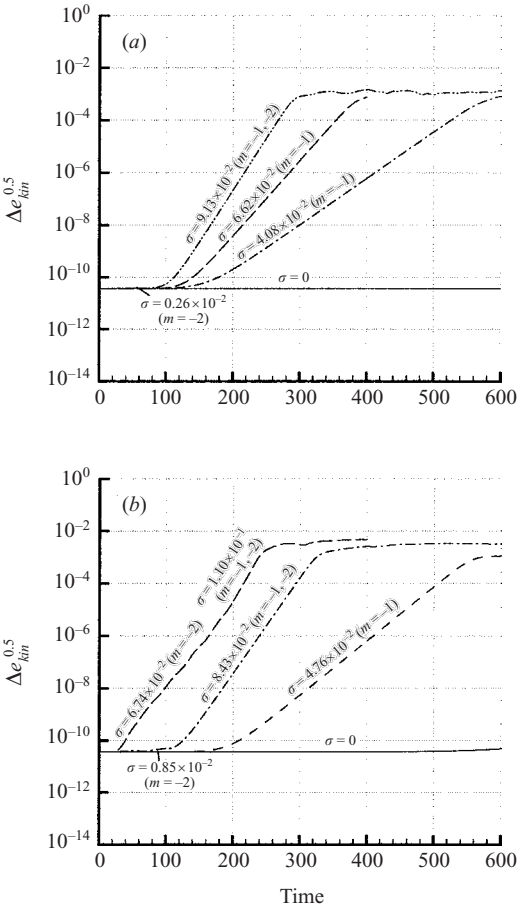

FIGURE 32. Growth rates σ: (*a*) $Re = 200$, $S = 1.095$, and different coflow. Solid line: $\alpha = 1.6$, the axisymmetric bubble breakdown base flow remains stable. Dash-dotted line: $\alpha = 1.2$, here the base flow becomes unstable toward $m = -1$ modes, ultimately rendering a helical breakdown structure. Dashed line: $\alpha = 1.0$, similar to $\alpha = 1.2$, although with larger exponential growth rate σ. Dash-dot-dotted line: $\alpha = 0.8$, exhibits two unstable modes $m = -1$ and $m = -2$ yielding a breakdown mode which switches between double and single helical. (*b*) $S = 1.3$, $\alpha = 1.0$, and different Reynolds number. Solid line: $Re = 100$, the axisymmetric bubble breakdown base flow remains stable. Dashed line: $Re = 120$, here the base flow becomes unstable toward $m = -1$ modes, ultimately rendering a helical breakdown structure. Dash-dotted line: $Re = 150$, exhibits two unstable modes $m = -1$ and $m = -2$ yielding a double-helical breakdown mode. Long-dashed line: $Re = 200$, similar to $Re = 150$, but with larger σ.

While the $m = -2$ mode grows exponentially with $\sigma = 3.31 \times 10^{-2}$ another mode with higher σ eventually takes over at approximately $t = 130$ (figure 28). Spectral analysis of a velocity signal reveals that this faster growing mode corresponds to $|m| = 1$. Hence one expects that an eigenfunction of the linearly superimposed modes exhibits a predominant $m = -1$ structure which is slightly modified by an $m = -2$ mode. Indeed, figure 31 confirms the existence of such a structure for $S = 1.2$ (frame *b*) while $S = 1.0$ (frame *a*), corresponding to $m = -1$ only exhibits two peaks in azimuth for a given axial position. Here, in contrast to the above-discussed cases, the λ_2-criterion of Jeong & Hussain (1995) (also discussed in § 3.2) has been used to educe the structure of the eigenfunction, since it has been found that it delivers a clearer

picture of the complex structure with widely varying $|\omega|$. Similar instability properties are obtained for the highest swirl parameter case $S = 1.3$ (figure 28) so that we conclude that the existence of the $m = -2$ instability mode causes a double-helical breakdown mode.

Figure 32(a) illustrates the effect of the coflow parameter α on the global growth rate σ and global mode m. Here, $Re = 200$ and $S = 1.095$ are kept constant, while α is varied to obtain jet-like ($\alpha > 1$) and wake-like ($\alpha < 1$) profiles. The strongest jet case $\alpha = 1.6$ remains stable, exhibiting an axisymmetric bubble breakdown mode, cf. § 3.3. Decreasing α to 1.2 renders the axisymmetric base flow unstable to $m = -1$ modes, ultimately rendering a helical breakdown structure. The reference case ($\alpha = 1.0$) undergoes a similar dynamical evolution; however its growth rate $\sigma = 6.62 \times 10^{-2}$ is larger. Finally, the wake-like profile $\alpha = 0.8$ exhibits two unstable modes $m = -1$ and $m = -2$, yielding a breakdown; mode which switches between double and single helical, much like the case $S = 1.2$ discussed above.

Finally, figure 32(b) shows the effect of the Reynolds number Re on the global growth rate σ and global mode m for a case with constant $S = 1.3$ and $\alpha = 1.0$. For the lowest Reynolds number, $Re = 100$, no helical instability is obtained and a stable axisymmetric bubble breakdown is obtained, cf. § 3.4. Increasing Re to $Re = 120$ renders the $m = -1$ mode unstable yielding a helical breakdown, while an even higher $Re = 150$ introduces two unstable modes ($m = -1$ and $m = -2$). The latter case subsequently gives rise to a double-helical breakdown mode. $Re = 200$ yields a similar double-helical breakdown; however the associated growth rates are larger.

6. Summary and conclusions

Preventing or benefiting from vortex breakdown in technical applications requires a thorough physical understanding of the various stages of the breakdown process, especially with regard to the influence of the boundary conditions. The main goal of the present investigation is to extend the present state of knowledge regarding onset, internal structure and mode selection of vortex breakdown, in order to facilitate controllability of the phenomenon.

For this purpose we perform axisymmetric and three-dimensional direct numerical simulations of spatially and temporally evolving swirling laminar jets and wakes in domains that are open in the downstream and radial directions. In order to address systematically the effects of unsteadiness and three-dimensionality on axisymmetric and helical vortex breakdown modes, we select a two-parametric velocity profile for which the steady axisymmetric breakdown is well-studied (Grabowski & Berger 1976). This allows us to present phenomenological observations, as well as mechanistic and theoretical explanations as function of the swirl S, the coflow α, and the Reynolds number Re.

The discussion commences with the presentation of a representative reference case ($S = 1.095$, $\alpha = 1$, and $Re = 200$). Since the axisymmetric columnar initial condition satisfies the steady Euler equations, viscous diffusion of axial vorticity away from the axis starts the evolution of the flow. This effectively reduces the induced velocity on the vortex axis, thereby increasing the pressure locally. Adverse pressure gradient and viscous diffusion yield a divergent vortex core, setting up a physical feedback mechanism that ultimately leads to vortex breakdown (Brown & Lopez 1990), despite the lack of an axial pressure gradient prescribed in the far field. The flow evolves toward an axisymmetric quasi-steady bubble breakdown state, enclosing an ovoid region of circulating fluid. The axisymmetric breakdown configuration eventually

becomes unstable to helical disturbances in the wake of the bubble, yielding a helical breakdown mode. Particles forming the helix are concentrated in low-pressure regions, although no local pressure minima can be observed, rendering pressure iso-surfaces inappropriate means to visualize the breakdown structure. In agreement with all reported accounts, the helical breakdown structure rotates with the ambient flow relative to the observer at a certain frequency for which a simple relation to S at the inflow plane is presented. Application of this estimate to the experimentally measured frequencies of Garg & Leibovich (1979) leads to good agreement with the present numerical investigation.

Simulations that differ from the reference case only in their applied swirl parameter S, show the existence of a critical swirl $S_c = 0.8944$ below which no internal stagnation point exists. The stable and axisymmetric breakdown at S_c is quickly replaced by a helical breakdown mode $m = -1$ as S takes larger values. Here the minus sign represents the fact that the winding sense of the helix is opposite to that of the flow. As the swirl parameter takes values larger than discussed for the reference case, the single helix is replaced by a pulsant double-helical breakdown mode $m = -2$. The wavenumber selection of the breakdown modes is verified by different means of visualization: passive particles, vorticity iso-surfaces and λ_2 iso-surfaces. For yet higher swirl $S = 1.6$, a two-celled axisymmetric quasi-steady bubble structure is observed, quickly superseded by an $m = -2$ breakdown mode. Large swirl values increase the tendency to local centrifugal instability and ultimately lead to counter-rotating vortex rings, as has already been suggested by Martin & Meiburg (1994). In this context, a comparison with the axisymmetric steady simulations allow us to determine whether they represent the averaged three-dimensional results. Note that the one- and two-celled internal structure of the bubble is not to be confused with a multiple bubble breakdown structure. The latter exhibits corotating vortices, substantially separated in the axial direction. Multiple breakdowns forming a bubble train are observed as a permanent feature only in axisymmetric calculations, since in three-dimensional simulations the bubble located further downstream quickly becomes unstable to helical disturbances, ultimately leading to helical breakdown modes.

The second independently varied parameter determines the characteristic of the axial velocity component. Wake-like profiles ($\alpha < 1$) exhibit an axial momentum deficit in the vortex core, which makes them more susceptible to vortex breakdown. As α decreases, helical breakdown modes with higher azimuthal wavenumber, i.e. $m = -1, -2$, respectively, are selected. Jet-like profiles ($\alpha > 1$) exhibit an increasing excess of axial momentum in the vortex core as α takes larger values, moving the most upstream stagnation point monotonically downstream. This effectively stabilizes the axisymmetric breakdown mode for sufficiently high α, such that no helical mode emerges until the simulations are stopped. For yet higher values of α, no breakdown is observed, in agreement with the momentum-balance model of Mahesh (1996). Note that, independent of the jet or wake character of the inflow profile, only negative helical winding senses are observed since the helices always originate in the wake of the breakdown bubble.

The effect of the Reynolds number Re on the existence, structure and mode selection of vortex breakdown is in many ways similar to that of S. The lowest Re considered leads to a viscous vortex core without exhibiting any sign of breakdown even for high swirl. Increasing Re leads to one axisymmetric breakdown bubble, which is superseded by two bubbles for even higher Re. Increasing Re further renders the flow temporally periodic, in agreement with the observed bifurcation sequence in closed cylinders (Escudier 1984, etc.). A similar bifurcation sequence leading to multiple breakdown

bubbles is obtained also for S. Further, as also observed for S, multiple breakdown bubbles are only transient features for the unconfined vortex considered here, being quickly superseded by helical breakdown modes. Provided sufficient swirl is applied, a clear sequence of mode selection $m = 0, -1, -2$ is obtained as Re is increased. For sufficiently large Reynolds numbers the bubble is completely destroyed, leaving a helical breakdown mode exhibiting an 'abrupt kink' similar to experimental observations.

The phenomenological observations summarized above confirm Benjamin's (1962) suggestion that the existence of vortex breakdown is explainable in terms of a steady axisymmetric model, although its mode selection is determined by the stability characteristics of the flow field created by the vortex breakdown itself (Escudier *et al.* 1982).

In this regard we show that a transition from super- to subcritical flow as defined by Benjamin (1962) accurately predicts the parameter combination yielding breakdown, if applied locally to a flow with supercritical inflow profile. Applying the criterion locally effectively renders the inviscid criterion viscous. The obtained criticality locus in the S, α parameter space agrees qualitatively with the result of Shi & Shan (1987), obtained from the failure of the quasi-cylindrical approximation which is governed by an equation differing from Benjamin's only by a viscosity-related term.

Consequently, the basic form of breakdown is axisymmetric, and a transition to helical breakdown modes is shown to be caused by a sufficiently large pocket of absolute instability (Huerre & Monkewitz 1990) in the wake of the bubble, giving rise to a self-excited global mode. The required size of the absolutely unstable pocket to sustain a global mode, however, is impossible to determine. For this reason we consider the global instability character of axisymmetric breakdown bubble flows with non-columnar velocity distribution along the axis. We determine exponential temporal growth rates for the helical-like instabilities, which are non-zero only for parameter combinations exhibiting helical breakdown modes and take larger values with increasing S and Re and decreasing α. Two distinct helical eigenfunctions corresponding to an azimuthal wavenumber $m = -1$ and $m = -2$ have been found to render a helical or double-helical breakdown mode, respectively.

An extension to top-hat jet flows with a very small amount of axial coflow as investigated by Billant, Chomaz & Huerre (1998) and Maxworthy (private communication) and typical for combustion and mixing applications is currently underway.

This work was supported in part by the National Science Foundation. The authors acknowledge several helpful discussions with J. M. Chomaz, J. M. Lopez and L. Redekopp. Furthermore, we thank R. Verzicco for his generosity in providing several subroutines of his code, and L. Redekopp for comments on an earlier draft.

REFERENCES

Althaus, W., Brücker, C. & Weimer, M. 1995*a* Breakdown of slender vortices. In *Fluid Vortices* (ed. S. Green), pp. 373–426. Kluwer.

Althaus, W., Krause, E., Hofhaus, J. & Weimer, M. 1995*b* Bubble- and spiral-type breakdown of slender vortices. *Expl Therm. Fluid Sci.* **11**, 276–284.

Batchelor, G. 1964 Axial flow in trailing line vortices. *J. Fluid Mech.* **20**, 645–658.

Beér, J. & Chigier, N. 1972 *Combustion Aerodynamics*. Applied Science Publishers.

Benjamin, T. 1962 Theory of the vortex breakdown phenomenon. *J. Fluid Mech.* **14**, 593–629.

Billant, P., Chomaz, J.-M. & Huerre, P. 1998 Experimental study of vortex breakdown in swirling jets. *J. Fluid Mech.* **376**, 183–219.

Bisset, D., Antonia, R. & Browne, L. 1990 Spatial organization of large structures in the turbulent far wake of a cylinder. *J. Fluid Mech.* **218**, 439–461.

Breuer, M. & Hänel, D. 1993 A dual time-stepping method for 3-D, viscous, incompressible vortex flows. *Computers Fluids* **22**, 467–484.

Brown, G. & Lopez, J. 1990 Axisymmetric vortex breakdown Part 2. Physical mechanisms. *J. Fluid Mech.* **221**, 553–576.

Brücker, C. 1993 Study of vortex breakdown by particle tracking velocimetry (PTV). Part 2: Spiral-type vortex breakdown. *Exps. Fluids* **14**, 133–139.

Brücker, C. & Althaus, W. 1992 Study of vortex breakdown by particle tracking velocimetry (PTV). Part 1: Bubble-type vortex breakdown. *Exps. Fluids* **13**, 339–349.

Chen, P. 2000 Numerical simulations of swirling flows. PhD thesis, Department of Aerospace and Mechanical Engineering, USC.

Chomaz, J., Huerre, P. & Redekopp, L. 1988 Bifurcations to local and global modes in spatially developing flows. *Phys. Rev. Lett.* **60**, 25–28.

Delbende, I., Chomaz, J.-M. & Huerre, P. 1998 Absolute/convective instabilities in the Batchelor vortex: a numerical study of the linear impulse response. *J. Fluid Mech.* **355**, 229–254.

Escudier, M. 1984 Observations of the flow produced in a cylindrical container by a rotating endwall. *Exps. Fluids* **2**, 189–196.

Escudier, M. 1988 Vortex breakdown: observations and explanations. *Prog. Aerospace Sci.* **25**, 189–229.

Escudier, M., Bornstein, J. & Maxworthy, T. 1982 The dynamics of confined vortices. *Proc. R. Soc. Lond.* A **382**, 335–360.

Escudier, M. & Zehnder, N. 1982 Vortex-flow regimes. *J. Fluid Mech.* **115**, 105–121.

Faler, J. & Leibovich, S. 1977 Disrupted states of vortex flow and vortex breakdown. *Phys. Fluids* **20**, 1385–1400.

Faler, J. & Leibovich, S. 1978 An experimental map of the internal structure of a vortex breakdown. *J. Fluid Mech.* **86**, 313–335.

Garg, A. & Leibovich, S. 1979 Spectral characteristics of vortex breakdown flowfields. *Phys. Fluids* **22**, 2053–2064.

Grabowski, W. & Berger, S. 1976 Solutions of the Navier–Stokes equations for vortex breakdown. *J. Fluid Mech.* **75**, 525–544.

Gursul, I. 1996 Effect of nonaxisymmetric forcing on a swirling jet with vortex breakdown. *Trans. ASME: J. Fluids Engng* **118**, 316–321.

Hall, M. 1972 Vortex breakdown. *Annu. Rev. Fluid Mech.* **4**, 195–218.

Huerre, P. & Monkewitz, P. 1990 Local and global instabilities in spatially developing flows. *Annu. Rev. Fluid Mech.* **22**, 473–537.

Hussain, A. & Hayakawa, M. 1987 Eduction of large-scale orgnized structures in a turbulent plane wake. *J. Fluid Mech.* **180**, 193–229.

Jeong, J. & Hussain, F. 1995 On the identification of a vortex. *J. Fluid Mech.* **285**, 69–94.

Kopecky, R. & Torrance, K. 1973 Initiation and structure of axisymmetric eddies in a rotating stream. *Computers Fluids* **1**, 289–300.

Krause, E. 1990 The solution to the problem of vortex breakdown. In *Twelfth Intl Conf. Numerical Methods in Fluid Dynamics* (ed. K. Morton), pp. 35–50. Lecture Notes in Physics, Springer.

Lambourne, N. & Bryer, D. W. 1961 The bursting of leading-edge vortices: Some observations and discussion of phenomenon. *Aero. Res. Council, R. & M.* 3282, p. 1.

Leibovich, S. 1978 The structure of vortex breakdown. *Annu. Rev. Fluid Mech.* **10**, 221–246.

Leibovich, S. & Kribus, A. 1990 Large-amplitude wavetrains and solitary waves in vortices. *J. Fluid Mech.* **216**, 459–509.

Leibovich, S. & Randall, J. 1973 Amplification and decay of long nonlinear waves. *J. Fluid Mech.* **53**, 481–493.

Lessen, M. & Paillet, F. 1974 The stability of a trailing vortex. Part 2. Viscous theory. *J. Fluid Mech.* **65**, 769–779.

Lessen, M., Singh, P. & Paillet, F. 1974 The stability of a trailing line vortex. Part 1. Inviscid theory. *J. Fluid Mech.* **63**, 753–763.

Lopez, J. 1990 Axisymmetric vortex breakdown. Part 1. Confined swirling flow. *J. Fluid Mech.* **221**, 533–552.

Lopez, J. & Perry, A. 1992 Axisymmetric vortex breakdown. Part 3. Onset of periodic flow and chaotic advection. *J. Fluid Mech.* **234**, 449–471.

Lucca-Negro, O. & O'doherty, T. 2001 Vortex breakdown: a review. *Prog. Energy Combust. Sci.* **27**, 431–481.

Ludwieg, H. 1960 Stabilität der Strömung in einem zylindrischen Ringraum. *Z. Flugwiss.* **8** (5), 135–140.

Ludwieg, H. 1962 Zur Erklärung der Instabilität der über angestellten Deltaflügeln auftretenden freien Wirbelkerne. *Z. Flugwiss.* **10** (6), 242–249.

Ludwieg, H. 1964 Experimentelle Nachprüfung der Stabilitätstheorien für reibungsfreie Strömungen mit schraubenlinienförmigen Stromlinien. *Z. Flugwiss.* **12** (8), 304–309.

Ludwieg, H. 1965 Erklärung des Wirbelaufplatzens mit Hilfe der Stabilitätstheorie für Strömungen mit schraubenlinienförmigen Stromlinien. *Z. Flugwiss.* **13** (12), 437–442.

Mager, A. 1972 Dissipation and breakdown of a wing-tip vortex. *J. Fluid Mech.* **55**, 609–628.

Mahesh, K. 1996 A model for the onset of breakdown in an axisymmetric compressible vortex. *Phys. Fluids* **8**, 3338–3345.

Marques, F. & Lopez, J. 2001 Precessing vortex breakdown mode in an enclosed cylinder flow. *Phys. Fluids* **13**, 1679–1682.

Martin, J. & Meiburg, E. 1994 The nonlinear evolution of swirling jets. *Meccanica* **29**, 331–341.

Maxworthy, T., Hopfinger, E. & Redekopp, L. 1985 Wave motion on vortex cores. *J. Fluid Mech.* **151**, 141–165.

Mitchell, A. & Délery, J. 2001 Research into vortex breakdown control. *Prog. Aerospace Sci.* **37**, 385–418.

Monkewitz, P. 1988 A note on vortex shedding from axisymmetric bluff bodies. *J. Fluid Mech.* **192**, 561–575.

Olendraru, C., Sellier, A., Rossi, M. & Huerre, P. 1996 Absolute/convective instability of the Batchelor vortex. *C.R. Acad. Sci. Paris* II b **323**, 153–159.

Olendraru, C., Sellier, A., Rossi, M. & Huerre, P. 1999 Inviscid instability of the Batchelor vortex: Absolute-convective transition and spatial branches. *Phys. Fluids* **11**, 1805–1820.

Pier, B. & Huerre, P. 2001 Nonlinear self-sustained structures and fronts in spatially developing wake flows. *J. Fluid Mech.* **435**, 145–174.

Randall, J. & Leibovich, S. 1973 The critical state: a trapped wave model of vortex breakdown. *J. Fluid Mech.* **58**, 495–515.

Rayleigh, Lord 1917 On the dynamics of revolving fluids. *Proc. R. Soc. Lond.* **93**, 148–154.

Reyna, L. & Menne, S. 1988 Numerical prediction of flow in slender vortices. *Computers Fluids* **16**, 239–256.

Ruith, M., Chen, P. & Meiburg, E. 2003 Development of boundary conditions for direct numerical simulations of three-dimensional vortex breakdown phenomena in semi-infinite domains. *Computers Fluids* (to appear).

Ruith, M. & Meiburg, E. 2002*a* Breakdown modes of swirling jets with coflow. (Winning entry from the 19th Annual Gallery of Fluid Motion exhibit.) *Phys. Fluids* **14**, S11.

Ruith, M. & Meiburg, E. 2002*b* Direct numerical simulation of spatially developing, three-dimensional swirling jets. *J. Turbul.* **3**, 1–8.

Rusak, Z. & Judd, K. 2001 The stability of noncolumnar swirling flows in diverging streamtubes. *Phys. Fluids* **13**, 2835–2844.

Saghbini, J. & Ghoniem, A. 1997 Numerical simulations of the dynamics and mixing in a swirling flow. *AIAA Paper* 97-0507.

Sarpkaya, T. 1971*a* On stationary and traveling vortex breakdowns. *J. Fluid Mech.* **45**, 545–559.

Sarpkaya, T. 1971*b* Vortex breakdown in swirling conical flows. *AIAA J.* **9**, 1792–1799.

Serre, E. & Bontoux, P. 2002 Vortex breakdown in a three-dimensional swirling flow. *J. Fluid Mech.* **459**, 347–370.

Shi, X. & Shan, X. 1987 Relation between the quasi-cylindrical approximation and the critical classification for swirling flow. *Vortex Control and Breakdown Behaviour, Second Intl Colloqu. on Vortical Flows*, pp. 72–82. BBC.

Snyder, D. & Spall, R. 2000 Numerical simulation of bubble-type vortex breakdown within a tube-and-vane apparatus. *Phys. Fluids* **12**, 603–608.

Spall, R., Gatski, T. & Ash, R. 1990 The structure and dynamics of bubble-type vortex breakdown. *Proc. R. Soc. Lond.* A **429**, 613–637.

Spall, R., Gatski, T. & Grosch, C. 1987 A criterion for vortex breakdown. *Phys. Fluids* **30**, 3434–3440.

Spall, R. & Snyder, D. 1999 Numerical simulations of vortex breakdown: Review and recent developments. *Recent Res. Devel. Heat, Mass Momentum Transfer* **2**, 41–70.

Verzicco, R. & Orlandi, P. 1996 A finite-difference scheme for three-dimensional incompressible flows in cylindrical coordinates. *J. Comput. Phys.* **123**, 402–414.

Yin, X.-Y., Sun, D.-J., Wei, M.-J. & Wu, J.-Z. 2000 Absolute and convective instability character of slender viscous vortices. *Phys. Fluids* **12**, 1062–1072.